RIS-Aided Protected Zone Formation for Physical Layer Security of In-Band Full Duplex Systems

Hanadi Salman, *Graduate Student Member, IEEE*, Abdulkadir Celik, *Senior Member, IEEE*, Sultangali Arzykulov, *Senior Member, IEEE*, Ahmed M. Eltawil, *Senior Member, IEEE*, and Hüseyin Arslan, *Fellow, IEEE*

***Abstract*—The rapid evolution of mobile technologies presents a formidable security challenge, as traditional cryptographic methods struggle to keep pace. Integrating physical layer security (PLS) solutions with cutting-edge technologies, such as in-band full-duplex (IBFD) and reconfigurable intelligent surfaces (RISs), holds promise for effectively addressing these challenges. This study introduces a novel RIS-driven protected zone (PZ) formation approach that employs artificial noise (AN) to safeguard legitimate users without requiring *a priori* knowledge of eavesdropper locations, channels, or numbers. The proposed methodology partitions the RIS into two distinct segments: while the former segment enhances the achievable data rate for the legitimate signal, the latter segment concurrently amplifies AN to jam illegitimate users within the PZ. We present formulations and solutions for maximizing secrecy capacity (SC) and minimizing power consumption through optimized transmit power allocation factors, RIS segmentation, and beams' directions, all subject to stringent quality-of-service (QoS) constraints. Closed-form expressions are derived to facilitate efficient implementation and performance optimization. Simulation results validate closed-form solutions and demonstrate that the proposed scheme can significantly enhance SC compared to benchmarks where RIS and AN are used separately, with the proposed scheme achieving approximately 81% greater capacity than the "RIS-Only" approach and a substantial advantage over the "AN-Only" approach, which results in no secrecy. Additionally, this work includes an analysis of energy efficiency, emphasizing the critical importance of optimizing power consumption in practical applications. This dual focus on improving security while effectively managing energy resources underscores the scheme's practical relevance and efficiency.**

***Index Terms*—Artificial noise, energy efficiency, full-duplex, optimization, partitioning, physical layer security, power control, reconfigurable intelligent surface, secrecy capacity.**

I. Introduction

THE fifth generation (5G) technology holds enormous potential as a cornerstone for the Internet-of-Everything. However, the swift progression towards fully intelligent and automated systems—encompassing industrial automation, augmented reality, virtual reality, flying vehicles, and connected autonomous systems—is likely to place substantial demands on 5G networks. These systems necessitate exceedingly high spectrum and energy efficiency, ultra-low latency, massive and ubiquitous wireless connectivity, comprehensive network coverage, and integrated intelligence, which may exceed the capabilities of 5G [1]. In response, both industry and academia are intensively researching sixth generation (6G) technology, that aims to address these technical challenges by delivering significantly improved key performance indicators [2], [3].

While the main focus for future wireless technologies revolves around achieving low latency and high reliability, a critical issue that persists is the security of sensitive information. The inherent broadcast nature of wireless communication makes it vulnerable to unauthorized access and eavesdropping [4], [5]. In an eavesdropping attack, the adversary continuously monitors the communication channel between the transmitter and the receiver to intercept legitimate transmission information. Traditional security mechanisms, including encryption and authentication, typically rely on the upper-layer network protocols. However, with the advent of more powerful computational resources available to attackers, conventional encryption techniques face significant security challenges. These challenges involve the development of more advanced encryption algorithms and the management of increasingly complex cryptographic keys [5]. Moreover, the rise of generative artificial intelligence technologies has further empowered attackers, enabling them to devise more sophisticated and potent attacks, which significantly escalates the security threat landscape [6]. Consequently, such advancements necessitate the continuous enhancement of current security measures to maintain the confidentiality and integrity of information in the face of evolving threats.

Physical layer security (PLS) effectively supplements traditional encryption techniques by exploiting the properties of the wireless channel, propagation environment, and communication systems. This approach ensures confidentiality by maintaining a higher quality of the legitimate communication link compared to that of an eavesdropper [7]. Reconfigurable intelligent surface (RIS) is emerging as a promising PLS technique [8], designed to enhance signal quality and coverage by manipulating the phase shifts of multiple passive reflecting elements, thereby altering wireless propagation paths. However, most existing studies on RIS primarily focus on either uplink (UL) or downlink (DL) transmissions, which can lead to sub-optimal utilization of spectrum and channel diversity. In-band

H. Salman and H. Arslan are with the Department of Electrical and Electronics Engineering, Istanbul Medipol University, Istanbul, 34810, Turkey. (e-mail: hanadi.suleiman@std.medipol.edu.tr, huseyinarslan@medipol.edu.tr)

A. Celik is with the School of Electronics and Computer Science, University of Southampton, Southampton SO17 1BJ, U.K. (e-mail: a.celik@soton.ac.uk)

S. Arzykulov is with the Department of Electrical and Computer Engineering, School of Engineering and Digital Sciences, Nazarbayev University, Astana, 010000, Kazakhstan. (e-mail: sultangali.arzykulov@nu.edu.kz)

A. M. Eltawil is with Computer, Electrical, and Mathematical Sciences & Engineering (CEMSE) Division at King Abdullah University of Science and Technology (KAUST), Thuwal, KSA. (e-mail: ahmed.eltawil@kaust.edu.sa)

full-duplex (IBFD) communication systems overcome this limitation by enabling simultaneous UL and DL transmissions on the same frequency band [9], effectively doubling spectrum efficiency. Integrating RIS with IBFD systems leverages the strengths of both technologies, allowing the RIS to function as a passive full-duplex (FD) reflector. This integration provides enhanced spectral efficiency and improved overall system performance. Building on this, this work focuses on leveraging IBFD to ensure robustness against eavesdropping by using DL transmission to secure UL communication. Specifically, we implement RIS partitioning strategy, where one segment of the RIS is configured to enhance the quality of the legitimate signal, while the other segment simultaneously amplifies artificial noise (AN) to disrupt illegitimate receivers. However, this integration presents challenges, particularly regarding the configuration of RIS, which necessitates knowledge of the eavesdropper's channel information—*a priori* information that is typically unavailable. This work addresses these challenges by developing robust optimization techniques to overcome these limitations, ensuring enhanced security in wireless transmissions.

A. Related Works

1) Artificial Noise: AN techniques have been extensively investigated in various PLS systems as a potent strategy to enhance secrecy rates [10]. Typically, the AN signal is combined with the information signal, and the total transmit power is distributed between them using an appropriate power allocation scheme. AN can be generated randomly with minimal computational complexity or strategically placed in the null space of a legitimate communication link to optimize its effectiveness [11]. For instance, [12] introduced the concept of adding artificial noise to the transmitted signal under the assumption that the eavesdropper's channel state information (CSI) is known. Additionally, [13] proposed noise-loop modulation as a method to ensure secure and reliable communications. This technique involves deliberately introducing noise into the channel, effectively jamming the transmission and preventing the illegitimate node from receiving the information, regardless of its computational power. In [14], the utilization of AN on the receiver side aims to establish a secure region. This approach defines the concept of outage secrecy region, where leakage probabilities are calculated based on positions within the region. The authors in [15] emphasized the critical need for AN in networks assisted by RIS. They argued that traditional beamforming techniques, whether for transmission or reflection, are inadequate in scenarios with multiple eavesdroppers due to limited spatial degrees of freedom. AN was proposed as an effective strategy to function as a transmit jammer under such challenging conditions, thereby significantly enhancing the secrecy capacity (SC) of the network.

2) Reconfigurable Intelligent Surfaces: RIS technology exhibits several distinctive characteristics that make it highly advantageous in wireless communication systems. Notably, RIS is nearly passive and unaffected by receiver noise. Its ease of deployment and minimal signal processing requirements further contribute to its appeal [16]. These features of RIS technology play a pivotal role in improving quality-of-service (QoS) metrics such as high data rates, support for numerous users, and ultra-high reliability [17]. Integrating RIS with PLS methods has been proposed to bolster secure communications among legitimate users [18]. For instance, in [19], the authors optimized the secrecy rate of RIS-assisted multi-antenna wireless systems using alternating optimization techniques. In [20], a joint beamforming and jamming strategy leveraging RIS improved secrecy rate even when the eavesdropper's CSI was unknown to the transmitter. Moreover, [21] provided asymptotic secrecy outage probability analysis, highlighting that increasing the number of RIS reflecting elements and average signal-to-interference-plus-noise ratio (SINR) enhances secrecy performance. Several articles have discussed the integration of RIS in PLS frameworks for various wireless networks [22], [23]. For example, [22] conducted a survey on RIS-assisted PLS research and highlighted open challenges in this area. Furthermore, [23] analyzed security and privacy challenges in RIS-assisted 6G technologies.

3) Full-Duplex Communication: FD communication systems have the potential to double spectral efficiency compared to half-duplex systems [24]. The primary challenge associated with FD systems is the substantial self-interference (SI) resulting from the leakage of transmitted signals into the received signals at the FD node. To make such a system more practical, advanced SI cancellation (SIC) techniques are critical and have been the focus of significant research. Studies, including the work presented in [25], have demonstrated that effective SIC can be achieved through various approaches. These approaches include the combination of antenna separation with digital cancellation, the integration of antenna separation with analog cancellation, and a hybrid approach utilizing antenna separation along with both analog and digital cancellation techniques. In [14], an intriguing study examined the transmission of AN by an FD receiver. RIS-aided FD systems have also garnered considerable attention for their potential in various applications, such as sum rate maximization [26] and transmit power minimization [27]. The study in [28] employed deep reinforcement learning to maximize the sum secrecy rate. In [29], the authors analyzed an RIS-aided FD system. The primary objective is to maximize the sum secrecy rate by jointly optimizing the transmit beamforming, receive beamforming, and AN covariance matrix at the FD-base station (BS), as well as the passive beamforming at the RIS.

B. Main Contributions

This work proposes a novel RIS-driven protected zone (PZ) formation approach that leverages RIS and AN to jam the legitimate user surroundings without depending on any *a priori* knowledge of eavesdropper locations, numbers, and channels. To this aim, the RIS is virtually split into two disjoint segments: the former enhances the achievable rate for the legitimate user, whereas the latter concurrently amplifies the AN to effectively jam any illegitimate users located anywhere within the PZ. The principal contribution of this paper, in comparison to the existing literature on AN-RIS-assisted PLS, is summarized in Table I, while a detailed enumeration of the

TABLE I: Comparative Analysis of the Paper's Contributions and Existing Literature

Ref.	Full-Duplex Transmission	RIS Partitioning	Passive Eavesdropper	Multiple Eavesdroppers	Secrecy Capacity Optimization	Energy Efficiency Optimization
[20]	✗	✗	✓	✗	✓	✗
[29]	✓	✗	✗	✗	✓	✗
[30]	✗	✓	✗	✗	✓	✓
[33]	✗	✓	✗	✓	✓	✗
This paper	✓	✓	✓	✓	✓	✓

comprehensive contributions are presented in the subsequent text.

- *RIS Partitioning and PZ Formation:* Inspired by the concept of virtual partitioning [30], the proposed scheme segments the RIS into distinct portions for UL and DL transmissions, which improves intended signal and AN at the BS and illegitimate users, respectively. The latter segment is further divided into sub-segments to amplify AN across a predefined PZ surrounding the legitimate user. We derive closed-form expressions for optimal RIS partitions and power allocation factors aimed at maximizing overall SC or minimizing power consumption. These optimizations are subject to stringent QoS constraints.
- *Practical Eavesdropping Model:* Recognizing the impracticality of presuming known eavesdropper location and channel information [10] or presupposing eavesdropper-free areas [31], the proposed scheme operates under an entirely passive eavesdropping paradigm and can accommodate eavesdroppers located within the PZ without the need for any *a priori* information. Moreover, in acknowledging the prevalence of multiple eavesdroppers in practical applications, the system model diverges from prior works [30], [32] by assuming the existence of multiple eavesdroppers, aligning more closely with real-world deployment scenarios.
- *Performance Enhancement:* This work significantly advances the security of wireless networks by integrating and optimizing the use of RIS and AN. Unlike previous approaches that apply RIS and AN independently without optimization, our proposed scheme achieves a superior security level. Specifically, simulation results demonstrate that our method enhances SC by approximately 81% compared to "RIS-Only" approaches and offers a substantial advantage over "AN-Only" approaches, which fail to improve SC. Additionally, our scheme is energy-efficient, reducing the power consumption by 3.59 dBm when relaxing the restriction on the achievable rate within the PZ from 1% to 10% of the legitimate data rate. This makes our solution not only more secure but also more viable for practical applications.

C. Paper Notations and Organization

This paper is structured as follows: Section II provides a detailed exposition of the network, channel, and signal models. Section III formulates the general optimization problem and outlines the associated solution methodology. Section IV investigates the optimization of power allocation and RIS partitioning, considering feasibility, maximum SC, and energy efficiency regimes. Section V focuses on optimizing beam boresight placement and details the solution approach. Section VI evaluates the effectiveness of the proposed scheme, with simulation results confirming the validity of the derived closed-form solutions. Finally, Section VII encapsulates the conclusions drawn and insights derived from this study.

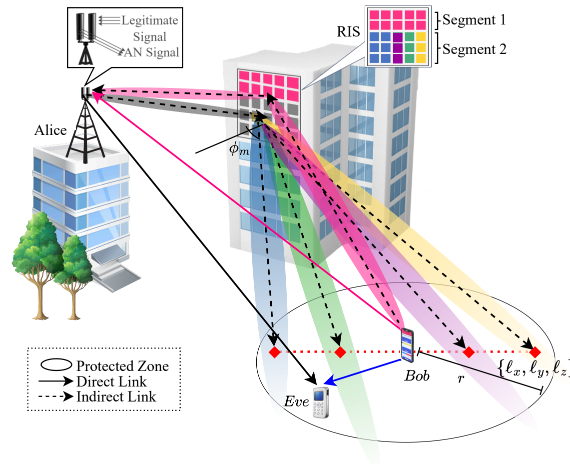

Fig. 1: System model under consideration with $M = 4$.

Notation: Scalars, vectors, and matrices are denoted by italic letters a, bold italic lower case letters $\boldsymbol{a}$, and bold italic capital letters $\boldsymbol{A}$, respectively. The operator $(\cdot)^T$ denotes the transpose. The floor operation is denoted by $\lfloor \cdot \rfloor$. For a vector, $\boldsymbol{a}(n)$ represents the n-th element of the vector $\boldsymbol{a}$. For complex numbers, $\Re(\cdot)$ and $\Im(\cdot)$ denote the real and imaginary parts, respectively. The phase of a complex number is indicated by $\angle(\cdot)$, and the norm operation is denoted by $|\cdot|$. The symbol $\jmath$ is used to represent the imaginary unit. For a variable, $\hat{x}$ denotes a fixed value, while $\overset{\star}{x}$ represents its optimal value. For clarity, the definitions of the parameters and notations are stated in Table II.

II. System Model

Consider a wireless communication system with an FD-BS (Alice), a single-antenna user (Bob), multiple single-antenna passive eavesdroppers (Eves), and N-element RIS as shown in Fig. 1. Alice has a single antenna for receiving the legitimate signal from Bob and a single antenna for simultaneously transmitting AN signal to jam Eves [34]. Eves exist in random locations within a predefined circular area of radius r surrounding Bob, which is referred to as PZ(r).

TABLE II: Table of Notations

Notation	Description
N	Number of RIS elements, indexed by $1 \leq n \leq N$
M	Number of beams, indexed by $1 \leq m \leq M$
$Pz(r)$	Circular PZ of radius r
$h_{u,v}$	Channel between nodes u and v
f_c	Carrier frequency
$\mathcal{B}$	channel bandwidth [Hz]
ρ_0	RIS partitioning factor assigned for UL signal
ρ_m	RIS partitioning factor assigned for mth beam
$N_0 = \lfloor \rho_0 N \rfloor$	RIS elements assigned for UL signal, indexed by $1 \leq n_0 \leq N_0$
$N_m = \lfloor \rho_m N \rfloor$	RIS elements assigned to direct mth beam, indexed by $1 + \sum_{\hat{m}=0}^{m-1} N_{\hat{m}} \leq n_m \leq \sum_{\hat{m}=0}^{m} N_{\hat{m}}$.
ϕ_m	Boresight angle of mth beam
$\boldsymbol{\ell_m}$	Cartesian coordinates of mth beam boresight
θ_n	Phase shift of nth RIS element
σ_ζ^2	Power of residual SI
α	Alice's power allocation factor
β	Bob's power allocation factor
Q_Y	QoS threshold

The primary threat posed by these Eves is their intention to intercept and decode the UL transmission between Bob and Alice[1], exploiting the inherently broadcast nature of wireless communication. We aim to keep the SINR at Eves within the PZ below their detection threshold. By doing so, the risk of detection for any Eves outside the PZ is minimized and inherent security is established beyond the PZ.

Furthermore, the RIS with N reflecting elements is deployed to both improve Bob's performance and counteract potential eavesdropping by properly adjusting the reflection coefficients in terms of phase. To achieve this, the RIS is partitioned into two disjoint segments: one segment is configured to enhance Bob's UL transmission, while the second segment is adjusted to amplify AN from Alice to jam Eves. In the absence of specific information about the Eves' locations, numbers, and CSI, this segment is further subdivided into M partitions to cover the entire area, generating M beams whose boresight angles are defined as $\boldsymbol{\phi} = [\phi_1, \phi_2, \ldots, \phi_M]$, where ϕ_m is the boresight's angle of mth beam as shown in Fig. 1.

A. Channel Model

Assuming that the wireless signals are propagated in a non-dispersive and narrow-band channel, the pertinent mathematical representation for all channels is provided as follows [35][2]

$$h_{u,v} = \sqrt{\beta_{u,v}}\; e^{-\jmath 2\pi f_c \tau_{u,v}}, \tag{1}$$

where $h_{u,v}$ is the single-input single-output channel between the generic nodes u and v. Moreover, $\beta_{u,v}$, $\tau_{u,v}$, and f_c are the pathloss, the propagation delay, and the carrier frequency, respectively. Following the channel model in (1), we denote the equivalent UL channels of the Bob-RIS link, the RIS-Alice link, the Bob-Alice link, Bob-Eve link, Bob-mth beam[3] as follows; $\boldsymbol{h_{B,R}} \in \mathbb{C}^{1\times N}$, $\boldsymbol{h_{R,A}} \in \mathbb{C}^{N\times 1}$, $h_{B,A} \in \mathbb{C}^{1\times 1}$, $h_{B,E} \in \mathbb{C}^{1\times 1}$, $h_{B,m} \in \mathbb{C}^{1\times 1}$, respectively. Similarly, the equivalent DL channels; the Alice-RIS link, the RIS-Eve link, the RIS-mth beam link, the Alice-Eve link, the Alice-mth beam are denoted as follows; $\boldsymbol{h_{A,R}} \in \mathbb{C}^{1\times N}$, $\boldsymbol{h_{R,E}} \in \mathbb{C}^{N\times 1}$, $\boldsymbol{h_{R,m}} \in \mathbb{C}^{N\times 1}$, $h_{A,E} \in \mathbb{C}^{1\times 1}$, $h_{A,m} \in \mathbb{C}^{1\times 1}$, respectively. As Eves do not disclose any information about their channels, the channels $\boldsymbol{h_{R,E}}$ and $h_{A,E}$ remain entirely unknown to the legitimate communication parties.

The reflection coefficient vector of the RIS is given by [38]

$$\boldsymbol{p} = \upsilon[r_1 e^{\jmath\theta_1}, r_2 e^{\jmath\theta_2}, \ldots, r_N e^{\jmath\theta_N}]^T \tag{2}$$

where $r_n \in [0,1]$ and $\theta_n \in [0, 2\pi)$ are the absorption coefficient and the phase shift of the nth reflecting element, respectively; and $\upsilon \in (0,1]$ denotes the the reflection efficiency. As the RIS is a near-passive reflecting apparatus, we assume that the absorption coefficients satisfy $r_n = 1, \forall n \in \{1, 2, \ldots, N\}$ [39]. To implement the RIS partitioning technique, as detailed in [30], [33], we allocate $N_0 = \lfloor \rho_0 N \rfloor \in \mathbb{Z}^+$ RIS elements to improve the data of Bob. Conversely, $N_m = \lfloor \rho_m N \rfloor \in \mathbb{Z}^+$ RIS elements are allocated to enhance the jamming impact of AN onto Eves, ensuring that $N_0 + \sum_{m=1}^{M} N_m \leq N$[4] and $\rho_0 + \sum_{m=1}^{M} \rho_m = 1$. The phase shift $\theta_{n_0} \in [0, 2\pi)$ of element $n_0 \in \{1, \ldots, N_0\}$ is configured to be $-(\angle \boldsymbol{h_{B,R}}(n_0) + \angle \boldsymbol{h_{R,A}}(n_0))$, ensuring alignment with Bob-RIS-Alice cascaded channel, while mitigating the impact of their respective phases. In order to distribute AN across the PZ, we define beams boresight locations as $\boldsymbol{\mathcal{L}} = [\boldsymbol{\ell_1}, \boldsymbol{\ell_2}, \cdots, \boldsymbol{\ell_M}]$[5], where $\boldsymbol{\ell_m} = [\ell_x^m, \ell_y^m, \ell_z^m]$ represents the Cartesian coordinates of the mth beam's boresight. For a given location, $\boldsymbol{\ell_m}$, the phase shift $\theta_{n_m} \in [0, 2\pi)$ of element $n_m \in \mathcal{N}_m = \{1 + \sum_{\hat{m}=0}^{m-1} N_{\hat{m}}, \ldots, \sum_{\hat{m}=0}^{m} N_{\hat{m}}\}$ in the m-th RIS partition is expressed as [40]

$$\theta_{n_m} = 2\pi \left(f_c \mathcal{T} + \frac{1}{\lambda}\Omega_{A,R} + \frac{1}{\lambda}\Omega_{R,m} \right), \tag{3}$$

where $\mathcal{T} = \tau_{A,R} + \tau_{R,m}$ is the overall propagation delay of Alice-RIS-mth beam link, and λ is the wavelength. The term $\Omega_{u,v} = \boldsymbol{c_{n_m}} \boldsymbol{k}(\psi_{u,v}, \varphi_{u,v})$ where $\boldsymbol{c_{n_m}}$ is the Cartesian coordinates of n_m element. The wave vector $\boldsymbol{k}(\psi, \varphi) \in \mathbb{R}^{3\times 1}$ is given by [41]

$$\boldsymbol{k}(\psi, \varphi) = [\cos(\varphi)\sin(\psi),\; \cos(\varphi)\sin(\psi),\; \sin(\varphi)]^T \tag{4}$$

where ψ and φ are the azimuth and elevation angles, respectively.

[1]This work focuses on securing legitimate data transmission in the UL direction, from Bob to Alice.

[2]The adopted channel model is chosen to effectively illustrate the core concept of this work within the single-carrier narrowband framework. We acknowledge that extending the proposed approach to more practical scenarios would require substantial modifications to the design methodology. Such extensions are left for future investigation.

[3]The geometric channel model employed to characterize the channel from RIS to mth beam location ($\boldsymbol{\ell_m}$) is based on methodologies described in [36] and [37].

[4]To fully leverage the benefits of RIS, the remaining RIS elements, after allocating N_0 and N_m $\forall m$, are incorporated into N_0. Notably, the number of these additional elements is relatively small compared to N.

[5]Our objective is to optimize the boresight angle of each beam to ensure that the AN jamming power is effectively distributed across the PZ. These specific locations are introduced to facilitate the formulation of the optimization problem and the development of solution methodology. Additionally, they are essential for configuring the phase shifts of the RIS.

$$Y = \sqrt{\beta P_b}\Bigg[\underbrace{h_{B,A}}_{\text{direct link}} + \underbrace{\sum_{n_0=1}^{N_0} \boldsymbol{h_{B,R}}(n_0)\boldsymbol{p}(n_0)\boldsymbol{h_{R,A}}(n_0)}_{\text{aligned legitimate signal}} + \underbrace{\sum_{m=1}^{M}\sum_{n_m\in\mathcal{N}_m} \boldsymbol{h_{B,R}}(n_m)\boldsymbol{p}(n_m)\boldsymbol{h_{R,A}}(n_m)}_{\text{non-aligned legitimate signal}}\Bigg]s + \zeta + w_Y \tag{5}$$

$$Z = \sqrt{\beta P_b}\ h_{B,E}\ s + \sqrt{\alpha P_a}\Bigg[h_{A,E} + \sum_{n_0=1}^{N_0} \boldsymbol{h_{A,R}}(n_0)\boldsymbol{p}(n_0)\boldsymbol{h_{R,E}}(n_0) + \sum_{m=1}^{M}\sum_{n_m\in\mathcal{N}_m} \boldsymbol{h_{A,R}}(n_m)\boldsymbol{p}(n_m)\boldsymbol{h_{R,E}}(n_m)\Bigg]n + w_Z \tag{6}$$

$$\gamma_Y(\beta,\boldsymbol{\rho},\boldsymbol{\mathcal{L}}) = \frac{\beta P_b\ \left|h_{B,A} + \rho_0\sum_{n=1}^{N}\boldsymbol{h_{B,R}}(n)\boldsymbol{p}(n)\boldsymbol{h_{R,A}}(n) + \sum_{m=1}^{M}\rho_m\sum_{n=1}^{N}\boldsymbol{h_{B,R}}(n)\boldsymbol{p}(n)\boldsymbol{h_{R,A}}(n)\right|^2}{\sigma_\zeta^2+\sigma_Y^2} \tag{7}$$

$$\gamma_Z(\alpha,\beta,\boldsymbol{\rho},\boldsymbol{\mathcal{L}}) = \frac{\beta P_b\ \left|h_{B,E}\right|^2}{\alpha P_a\ \left|h_{A,E} + \rho_0\sum_{n=1}^{N}\boldsymbol{h_{A,R}}(n)\boldsymbol{p}(n)\boldsymbol{h_{R,E}}(n) + \sum_{m=1}^{M}\rho_m\sum_{n=1}^{N}\boldsymbol{h_{A,R}}(n)\boldsymbol{p}(n)\boldsymbol{h_{R,E}}(n)\right|^2 + \sigma_Z^2} \tag{8}$$

B. Signal Model

For the wireless system described above, the received signal at Alice can be expressed as shown in (5), wherein β and P_b denote the power allocation factor and maximum transmitted power from Bob, respectively; s is the legitimate signal transmitted from Bob; $\zeta \sim \mathcal{CN}(0,\sigma_\zeta^2)$ signifies the residual SI encountered at Alice[6]; and $w_Y \sim \mathcal{CN}(0,\sigma_Y^2)$ represents the complex additive white Gaussian noise (AWGN) characterized by zero mean and variance of σ_Y^2.

Furthermore, the received signal at any Eve can be expressed as in (6)[7], wherein α and P_a stand for the power allocation factor and maximum transmitted power attributed to Alice, respectively; n is the AN signal; and $w_Z \sim \mathcal{CN}(0,\sigma_Z^2)$ represents the complex AWGN characterized by zero mean and variance of σ_Z^2.

Assuming perfect pre-shared CSI, the SINR at Alice, γ_Y, can be expressed as in (7) taking into consideration that $\sum_{n=1}^{\lfloor\rho_0 N\rfloor}(\cdot) \approx \rho_0\sum_{n=1}^{N}(\cdot)$[8], where $\boldsymbol{\rho} = [\rho_0,\rho_1,\dots,\rho_M]$. Since we consider only N_0 RIS elements aligned with the Bob-RIS-Alice cascaded channel, the impact of non-aligned channels is disregarded as noted in [33, Fig. 2]. Consequently, γ_Y can be simplified as

$$\gamma_Y(\beta,\boldsymbol{\rho},\boldsymbol{\mathcal{L}}) = \frac{\beta P_b\ \left|h_{B,A} + \rho_0\sum_{n=1}^{N}\boldsymbol{h_{B,R}}(n)\boldsymbol{p}(n)\boldsymbol{h_{R,A}}(n)\right|^2}{\sigma_\zeta^2+\sigma_Y^2}. \tag{9}$$

[6]Even though developing SIC methods is beyond the scope of this study, the performance of the proposed approach has been evaluated under different residual SI power levels, as demonstrated in Figs. 6, 7, and 9c.

[7]This work is predicated on the assumption that no prior information about the eavesdroppers, including their location, number, or CSI, is available. Therefore, γ_Z is employed exclusively for performance evaluation purposes in Section VI.

[8]This assumption provides an approximation that becomes increasingly accurate, approaching equality as the number of elements N grows large. The accuracy of this approximation can be verified through numerical simulation results, which are presented in Section VI-A.

On the other hand, Eves remain uninformed about the presence of the AN and experience it as interference. Thus, the SINR at any Eve's location, γ_Z, can be expressed as in (8). Denoting channel bandwidth by $\mathcal{B}$, the legitimate data rate can be obtained as

$$R_Y(\beta,\boldsymbol{\rho},\boldsymbol{\mathcal{L}}) = \mathcal{B}\log(1+\gamma_Y(\beta,\boldsymbol{\rho},\boldsymbol{\mathcal{L}})), \tag{10}$$

while the achievable rate at illegitimate nodes can be expressed as

$$R_Z(\alpha,\beta,\boldsymbol{\rho},\boldsymbol{\mathcal{L}}) = \mathcal{B}\log(1+\gamma_Z(\alpha,\beta,\boldsymbol{\rho},\boldsymbol{\mathcal{L}})). \tag{11}$$

In the domain of PLS, the concept of SC quantifies the disparity in achievable information rates between legitimate and illegitimate entities, which can be mathematically expressed as

$$SC(\alpha,\beta,\boldsymbol{\rho},\boldsymbol{\mathcal{L}}) = [R_Y(\beta,\boldsymbol{\rho},\boldsymbol{\mathcal{L}}) - R_Z(\alpha,\beta,\boldsymbol{\rho},\boldsymbol{\mathcal{L}})]^+, \tag{12}$$

where $[x]^+ = \max(0,x)$.

III. PROBLEM FORMULATION AND SOLUTION METHODOLOGY

In this section, we will first provide formal problem formulations and then outline the solution methodology exploited in the subsequent sections.

A. Problem Formulation

We consider optimal PZ formation for RIS-aided IBFD systems considering following practical operational regimes: 1) Feasible regime, 2) Maximum SC regime, and 3) Energy efficiency regime. To reach these objectives of interest, we consider optimization of the following key system parameters:

- Alice's power allocation factor, α, that determines the AN's jamming impact and power consumed for Bob's protection,
- Bob's power allocation factor, β, impacting both data and eavesdropping rates,

$$\gamma_m(\alpha,\beta,\boldsymbol{\rho},\boldsymbol{\mathcal{L}}) = \frac{\beta P_b |h_{B,m}|^2}{\alpha P_a \left| h_{A,m} + \rho_m \sum_{n=1}^{N} \boldsymbol{h_{A,R}}(n)\boldsymbol{p}(n)\boldsymbol{h_{R,m}}(n)\right|^2 + \sigma_m^2} \tag{13}$$

- RIS partitioning factors, $\boldsymbol{\rho}$, regulating shape and gain of passive reflection beam shapes, thereby affecting the overall secrecy capacity.
- Boresight locations of the jamming beams reflected from RIS partitions, $\boldsymbol{\mathcal{L}}$, whose arrangement is a decisive factor of AN power distribution across the PZ.

All operational regimes are subject to the satisfaction of the following common constraints:

- The legitimate data rate is no less than a predefined threshold denoted as Q_Y.
- The achievable rate at $\boldsymbol{\mathcal{L}}$ remains below a specified threshold, defined as ηQ_Y, where $\eta \in [0,1]$.
- The summation of RIS portions does not exceed unity.

The optimization process is executed at Alice, where the optimal system parameters are computed. Upon obtaining these parameters, Alice conveys the RIS partitioning and beamforming configurations to the RIS controller, which subsequently adjusts the RIS accordingly. Furthermore, Alice informs Bob of the selected power allocation through a handshaking process, ensuring seamless coordination and efficient system operation.

In light of the above goals and criteria, we provide a generic problem formulation as follows

$$\mathbf{P}_{\boldsymbol{o}}: \max_{\alpha,\beta,\boldsymbol{\rho},\boldsymbol{\mathcal{L}}} \; f(\cdot) \tag{14a}$$
$$\text{s.t.} \quad \gamma_Y(\beta,\boldsymbol{\rho},\boldsymbol{\mathcal{L}}) \geq \overline{\gamma}_Y, \tag{14b}$$
$$\gamma_m(\alpha,\beta,\boldsymbol{\rho},\boldsymbol{\mathcal{L}}) \leq \overline{\gamma}, \forall m, \tag{14c}$$
$$\rho_0 + \sum_{m=1}^{M} \rho_m \leq 1, \tag{14d}$$
$$\boldsymbol{\mathcal{L}} \in \mathrm{PZ}(r), \tag{14e}$$
$$\{\alpha,\beta,\boldsymbol{\rho}\} \in [0,1], \tag{14f}$$

where the feasible regime takes an arbitrary constant as an objective function by definition of the feasibility problems [42]; the maximum SC regime sets $f \triangleq \overline{SC}(\alpha,\beta,\boldsymbol{\rho},\hat{\boldsymbol{\mathcal{L}}}) = [R_Y(\beta,\boldsymbol{\rho},\hat{\boldsymbol{\mathcal{L}}}) - \frac{1}{M}\sum_{m=1}^{M} R_m(\alpha,\beta,\boldsymbol{\rho},\hat{\boldsymbol{\mathcal{L}}})]^+$ as its goal[9], energy-efficiency regime sets $f \triangleq -(\alpha P_a + \beta P_b)$ where negation is introduced to keep generic maximization problem valid for the minimization of energy expenditure. Defining SINR at mth boresight location as in (13) with σ_m^2 representing the noise's variance, (14b) and (14c) constitute the QoS constraints, where $\overline{\gamma}_Y = 2^{Q_Y} - 1$ and $\overline{\gamma} = 2^{\eta Q_Y} - 1$ are the minimum required SINR thresholds. These thresholds are essential for maintaining reliable and secure communication in our study. In (14d), we ensure that the summation of RIS portions does not exceed unity to limit the total number of exploited RIS elements to not be higher than the total number of RIS elements. Finally, (14e) and (14f) specify the domain of optimization variables.

[9]The data rate at the mth boresight location is given by $R_m(\alpha,\beta,\boldsymbol{\rho},\hat{\boldsymbol{\mathcal{L}}}) = \mathcal{B}\log(1+\gamma_m(\alpha,\beta,\boldsymbol{\rho},\hat{\boldsymbol{\mathcal{L}}}))$.

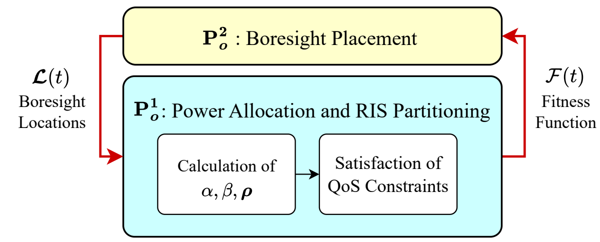

Fig. 2: Schematic illustration of the solution methodology.

B. Solution Methodology

In order to solve the generic problem formulated in (14), we follow a block coordinate descent (BCD) approach as shown in Fig. 2. In the first stage of each iteration, we fix the boresight locations of the passive reflective beams to predetermined locations denoted by $\hat{\boldsymbol{\mathcal{L}}}$. In this case, the first sub-problem can be formulated as

$$\mathbf{P}_{\boldsymbol{o}}^{\mathbf{1}}: \max_{\alpha,\beta,\boldsymbol{\rho}} \; f(\cdot) \tag{15a}$$
$$\text{s.t.} \quad \gamma_Y\left(\alpha,\beta,\boldsymbol{\rho},\hat{\boldsymbol{\mathcal{L}}}\right) \geq \overline{\gamma}_Y, \tag{15b}$$
$$\gamma_m\left(\alpha,\beta,\boldsymbol{\rho},\hat{\boldsymbol{\mathcal{L}}}\right) \leq \overline{\gamma}, \forall m, \tag{15c}$$
$$\rho_0 + \sum_{m=1}^{M} \rho_m \leq 1, \tag{15d}$$
$$\{\alpha,\beta,\boldsymbol{\rho}\} \in [0,1], \tag{15e}$$

which will be solved in closed-form in the subsequent sections to obtain optimal solutions at $\hat{\boldsymbol{\mathcal{L}}}$, i.e., $\overset{\star}{\alpha}(\hat{\boldsymbol{\mathcal{L}}})$, $\overset{\star}{\beta}(\hat{\boldsymbol{\mathcal{L}}})$, and $\overset{\star}{\boldsymbol{\rho}}(\hat{\boldsymbol{\mathcal{L}}})$ for feasibility, maximum SC, and energy efficient regimes in Section IV-A, Section IV-B, and Section IV-C, respectively. In the second stage, conditional optimal variables are employed in the boresight location search problem that is formulated as

$$\mathbf{P}_{\boldsymbol{o}}^{\mathbf{2}}: \max_{\boldsymbol{\mathcal{L}}} \; f(\cdot) \tag{16a}$$
$$\text{s.t.} \quad \gamma_Y\left(\overset{\star}{\alpha}(\boldsymbol{\mathcal{L}}),\overset{\star}{\beta}(\boldsymbol{\mathcal{L}}),\overset{\star}{\boldsymbol{\rho}}(\boldsymbol{\mathcal{L}})\right) \geq \overline{\gamma}_Y, \tag{16b}$$
$$\gamma_m\left(\overset{\star}{\alpha}(\boldsymbol{\mathcal{L}}),\overset{\star}{\beta}(\boldsymbol{\mathcal{L}}),\overset{\star}{\boldsymbol{\rho}}(\boldsymbol{\mathcal{L}})\right) \leq \overline{\gamma}, \forall m, \tag{16c}$$
$$\boldsymbol{\mathcal{L}} \in \mathrm{PZ}(r). \tag{16d}$$

The issue of determining optimal boresight locations is a complex optimization problem, which involves a large search space. In such cases, traditional optimization methods may struggle to find the global optimum or may become computationally expensive. To address this challenge, heuristic search algorithms, such as simulated annealing (SA) and particle swarm optimization, can be employed as detailed in Section V.

IV. Optimal Power Allocation and RIS Partitioning

In this section, we will focus on solving $\mathbf{P_o^1}$ in (15) and provide closed-form[10] derivations of power allocation and RIS partitioning for a given boresight location for operational regimes of interest.

A. Feasible Regime

This section focuses on deriving the feasibility constraints that demonstrate the practical viability of the aforementioned optimization problems. These constraints establish foundational thresholds for the minimum acceptable power allocation factors, crucial for ensuring the robustness and efficacy of the optimization strategies. Accordingly, the following lemmas provide the feasible ranges of power allocation and RIS partitioning variables that satisfy QoS constraints for the total number of RIS elements.

Lemma 1: For given power allocations and boresight locations (i.e., $\hat{\alpha}$, $\hat{\beta}$, and $\hat{\boldsymbol{\mathcal{L}}}$), the RIS portions satisfying QoS constraint $\gamma_m(\hat{\alpha},\hat{\beta},\boldsymbol{\rho},\hat{\boldsymbol{\mathcal{L}}}) \leq \overline{\gamma}, \forall m$, at boresight locations are given by

$$\overset{\star}{\rho}_m(\hat{\alpha},\hat{\beta},\hat{\boldsymbol{\mathcal{L}}}) \geq \frac{-c_m + \sqrt{\frac{\hat{\beta}P_b(a_m^2+b_m^2)}{\hat{\alpha}P_a\overline{\gamma}} - \frac{\sigma_m^2}{\hat{\alpha}P_a} - d_m^2}}{g_m}, \tag{17}$$

whose terms are obtained from the following expressions $h_{B,m} = a_m + \jmath b_m$, $h_{A,m} = c_m + \jmath d_m$, and $g_m = \sum_{n=1}^N \boldsymbol{h_{A,R}}(n)\boldsymbol{p}(n)\boldsymbol{h_{R,m}}(n)$, where $a_m, b_m, c_m, d_m, g_m \in \mathbb{R}, \forall m$. Likewise, the RIS portion satisfying QoS constraint of legitimate transmission, $\gamma_Y(\hat{\beta},\boldsymbol{\rho},\hat{\boldsymbol{\mathcal{L}}}) \geq \overline{\gamma}_Y$, is given by

$$\overset{\star}{\rho}_0(\hat{\beta},\hat{\boldsymbol{\mathcal{L}}}) \geq -\frac{q}{l} + \sqrt{\frac{\overline{\gamma}_Y(\sigma_\zeta^2+\sigma_Y^2) - \beta P_b k^2}{\beta P_b l^2}}, \tag{18}$$

where $h_{B,A} = q + \jmath k$ and $\sum_{n=1}^N \boldsymbol{h_{B,R}}(n)\boldsymbol{p}(n)\boldsymbol{h_{R,A}}(n) = l$ with $q, k, l \in \mathbb{R}$.

Proof 1: Please see Appendix A. ∎

Notice that the validity of (17) and (18) is subject to the satisfaction of constraint in (15d), i.e., $\overset{\star}{\rho}_0(\hat{\beta},\hat{\boldsymbol{\mathcal{L}}}) + \sum_{m=1}^M \overset{\star}{\rho}_m(\hat{\alpha},\hat{\beta},\hat{\boldsymbol{\mathcal{L}}}) \leq 1$, from which we obtain the minimum power allocation factors in the following lemmas.

Lemma 2: For a given $\hat{\beta}$, the minimum AN power allocation factor that satisfies $\overset{\star}{\rho}_0(\hat{\beta},\hat{\boldsymbol{\mathcal{L}}}) + \sum_{m=1}^M \overset{\star}{\rho}_m(\alpha,\hat{\beta},\hat{\boldsymbol{\mathcal{L}}}) \leq 1$ is given by

$$\alpha_{\min}(\hat{\beta}) = \left(\frac{\sum_{m=1}^M \sqrt{\frac{\hat{\beta}P_b(a_m^2+b_m^2)-\overline{\gamma}\sigma_m^2}{\overline{\gamma}P_a g_m^2}}}{1 + \frac{q}{l} + \sum_{m=1}^M \frac{d_m+c_m}{g_m} - \Gamma}\right)^2, \tag{19}$$

where $\Gamma = \sqrt{\frac{\overline{\gamma}_Y(\sigma_\zeta^2+\sigma_Y^2)-\hat{\beta}P_b k^2}{\hat{\beta}P_b l^2}}$.

Proof 2: Please see Appendix A. ∎

At this point, it is worth noting that the highest feasible AN transmit power at Alice is unity since γ_m attains its minimum value as $\alpha \to 1$; which serves as the feasible upper bound. Likewise, the next lemma obtains Bob's transmit power that satisfies QoS constraints subject to optimal RIS portions obtained in Lemma 1.

Lemma 3: For a given $\hat{\alpha}$, the minimum Bob's power allocation factor that satisfies $\overset{\star}{\rho}_0(\beta,\hat{\boldsymbol{\mathcal{L}}}) + \sum_{m=1}^M \overset{\star}{\rho}_m(\hat{\alpha},\beta,\hat{\boldsymbol{\mathcal{L}}}) \leq 1$ is given by

$$\beta_{\min}(\hat{\alpha}) = \left(\frac{-\Lambda + \sqrt{\Lambda^2 - 4\sqrt{\frac{\overline{\gamma}_Y(\sigma_\zeta^2+\sigma_Y^2)}{P_b l^2}}\sum_{m=1}^M \sqrt{\frac{u_m}{g_m^2}}}}{2\sum_{m=1}^M \sqrt{\frac{u_m}{g_m^2}}}\right)^2, \tag{20}$$

where $\Lambda = 1 + \frac{q+k}{l} + \sum_{m=1}^M \frac{c_m+d_m}{g_m} + \sum_{m=1}^M \sqrt{\frac{\sigma_m^2}{\hat{\alpha}P_a g_m^2}}$, and $u_m = \frac{P_b(a_m^2+b_m^2)}{\overline{\gamma}\hat{\alpha}P_a}$.

Proof 3: Please see Appendix A. ∎

B. Maximum SC Regime

In this section, we consider the maximum SC regime as formulated in (15) with the objective function $f = \gamma_{SC}(\alpha,\beta,\boldsymbol{\rho},\hat{\boldsymbol{\mathcal{L}}})$. To this aim, the utilization of all RIS elements is required to maximize the SC. Consequently, constraint in (15d) must be satisfied with equality at the optimal point, i.e.,

$$\overset{\star}{\rho}_0(\overset{\star}{\beta},\hat{\boldsymbol{\mathcal{L}}}) + \sum_{m=1}^M \overset{\star}{\rho}_m(\overset{\star}{\alpha},\overset{\star}{\beta},\hat{\boldsymbol{\mathcal{L}}}) = 1, \tag{21}$$

where $\overset{\star}{\alpha}$ and $\overset{\star}{\beta}$ represent optimal power allocation factors. The optimal solution further dictates $\overset{\star}{\alpha} = 1$ that will maximize AN power and minimize RIS portions allocated for jamming, thereby leaving rest of RIS portions to be utilized for Bob. In what follows, we focus on optimal power allocation for Bob and finally provide optimal closed-form RIS portions.

Lemma 4: Since $\gamma_Y(\beta,\boldsymbol{\rho},\hat{\boldsymbol{\mathcal{L}}})$ is a faster monotonically increasing function of β than $\gamma_m(\alpha,\beta,\boldsymbol{\rho},\hat{\boldsymbol{\mathcal{L}}})$, $\gamma_{SC}(\alpha,\beta,\boldsymbol{\rho},\hat{\boldsymbol{\mathcal{L}}})$ is non-negative and monotonically increases with β. Hence, the optimal Bob's transmit power that maximizes $\gamma_{SC}(\alpha,\beta,\boldsymbol{\rho},\boldsymbol{\mathcal{L}})$ is given by $\overset{\star}{\beta} = 1$.

Proof 4: Please see Appendix B

Accordingly, following corollary provides closed-form RIS partitions for maximum SC regime.

Corollary 1: The optimal RIS portions that maximize SC at boresight locations are given by

$$\overset{\star}{\rho}_m(\hat{\boldsymbol{\mathcal{L}}}) = \frac{-c_m + \sqrt{\frac{P_b(a_m^2+b_m^2)}{P_a\overline{\gamma}} - \frac{\sigma_m^2}{P_a} - d_m^2}}{g_m}, \tag{22}$$

which is obtained by substituting optimal power allocation factors, $\overset{\star}{\alpha} = \overset{\star}{\beta} = 1$, into (17), i.e., $\overset{\star}{\rho}_m(1,1,\hat{\boldsymbol{\mathcal{L}}})$. Since all

[10]The closed-form solutions derived in this work are applicable to any channel model, as the channel is treated as a given parameter. For instance, in the case of a multipath channel, the channel can be expressed as $\sum_{i=1}^L x_i + \jmath y_i$., where L denotes the number of propagation paths. With appropriate adaptations, these solutions can be extended to more complex channel conditions.

Algorithm 1: Beam Boresight Placement

Input: environmental parameters;
$Temp \leftarrow$ Initialize the temperature;
$\mathcal{L}(0) \leftarrow$ Initialize the boresight locations;
$\mathcal{F}(0) \leftarrow \mathbf{P}_o^1(\mathcal{L}(0))$ *// Evaluate the initial location*
$\overset{\star}{\mathcal{L}} \leftarrow \mathcal{L}(0)$ *// Set the best location*
$\overset{\star}{\mathcal{F}} \leftarrow \mathcal{F}(0)$ *// Set the best fitness function*
for $t = 1 : T$ **do**
  $\mathcal{L}(t) \leftarrow$ Pick a new boresight location
  $\mathcal{F}(t) \leftarrow \mathbf{P}_o^1(\mathcal{L}(t))$ *// Evaluate fitness of* $\mathcal{L}(t)$
  if $\mathcal{F}(t) \geq \mathcal{F}(t-1)$ **then**
    $\overset{\star}{\mathcal{F}} \leftarrow \mathcal{F}(t)$
    if $\mathcal{F}(t) \geq \overset{\star}{\mathcal{F}}$ **then**
      $\overset{\star}{\mathcal{F}} \leftarrow \mathcal{F}(t)$
  else
    if $\exp\left\{-\frac{\mathcal{F}(t)-\mathcal{F}(t-1)}{Temp}\right\} > rand$ **then**
      $\overset{\star}{\mathcal{F}} \leftarrow \mathcal{F}(t)$
  $Temp \leftarrow \frac{Temp}{i+1}$ \\ Decrease temperature;
return $\overset{\star}{\mathcal{L}}, \overset{\star}{\mathcal{F}}$;
Procedure $\mathbf{P}_o^1(\mathcal{L}(t))$:
Input: $\mathcal{L}(t)$;
$\alpha(\overset{\star}{\mathcal{L}}(t)) \leftarrow$ Calculate Alice's transit power factor;
$\beta(\overset{\star}{\mathcal{L}}(t)) \leftarrow$ Calculate Bob's transit power factor;
for *m=1:M* **do**
  $\overset{\star}{\rho}_m(\mathcal{L}(t)) \leftarrow$ Calculate AN's RIS portion (17);
$\overset{\star}{\rho}_0 \leftarrow 1 - \sum_{m=1}^{M} \overset{\star}{\rho}_m$ *// Calculate Bob's RIS portion*
if $\overset{\star}{\rho}_0 + \sum_{t=1}^{M} \overset{\star}{\rho}_m \leq 1$ **then**
  $\overset{\star}{f}(\overset{\star}{\alpha}, \overset{\star}{\beta}, \overset{\star}{\rho}, \mathcal{L}(t)) \leftarrow$ Calculate fitness/objective function
  if $\gamma_Y(\overset{\star}{\beta}, \overset{\star}{\rho}, \mathcal{L}(t)) < \overline{\gamma}_Y \vee \gamma_m(\overset{\star}{\alpha}, \overset{\star}{\beta}, \overset{\star}{\rho}, \mathcal{L}(t)) > \overline{\gamma}_m$ **then**
    $\overset{\star}{f}(\overset{\star}{\alpha}, \overset{\star}{\beta}, \overset{\star}{\rho}, \mathcal{L}(t)) \leftarrow 0$
else
  $\overset{\star}{f}(\overset{\star}{\alpha}, \overset{\star}{\beta}, \overset{\star}{\rho}, \mathcal{L}(t)) \leftarrow 0$
$\mathcal{F}(t) \leftarrow \overset{\star}{f}(\overset{\star}{\alpha}, \overset{\star}{\beta}, \overset{\star}{\rho}, \mathcal{L}(t))$;
return $\mathcal{F}(t)$;
end procedure;

RIS elements must be utilized for the maximum SC, the optimal RIS portion allocated for Bob is given by $\overset{\star}{\rho}_0(\hat{\mathcal{L}}) = 1 - \sum_{m=1}^{M} \overset{\star}{\rho}_m(\hat{\mathcal{L}}) \geq -\frac{q}{l} + \sqrt{\frac{\overline{\gamma}_Y(\sigma_\zeta^2+\sigma_Y^2)-P_b k^2}{P_b l^2}}$. If this condition is not met, $\overset{\star}{\rho}_0(\hat{\mathcal{L}})$ is set to $-\frac{q}{l} + \sqrt{\frac{\overline{\gamma}_Y(\sigma_\zeta^2+\sigma_Y^2)-P_b k^2}{P_b l^2}}$. This adjustment ensures that both constraints (15b) and (15c) are satisfied.

C. Energy Efficiency Regime

In addition to addressing security concerns, energy efficiency in wireless systems is crucial for ensuring sustainable and efficient operation [43], thereby enhancing overall network performance and resource utilization. This section aims at minimizing total power consumption, i.e., $f \triangleq -(\alpha P_a + \beta P_b)$, through joint optimization of power allocation factors and RIS portions subject to QoS constraints. The objective is to formulate an optimization problem that balances power efficiency with stringent QoS requirements. Specifically, the problem is expressed as given in (15). In order to minimize the overall power consumption, QoS constraints must be satisfied at equality as providing a higher and lower rate for legitimate and illegitimate transmissions, respectively, necessitates unnecessarily more power consumption. On the other hand, RIS elements must be fully exploited to minimize the burden on power allocation factors. In light of these remarks, following lemmas provide solution for energy-efficient PZ formation operation.

Lemma 5: For a given $\hat{\alpha}$ and $\hat{\mathcal{L}}$, Bob's optimal power allocation factor can be obtained by solving $\rho_0(\beta, \hat{\mathcal{L}}) + \sum_{m=1}^{M} \rho_m(\hat{\alpha}, \beta, \hat{\mathcal{L}}) = 1$ for β as follows

$$\overset{\star}{\beta}(\hat{\alpha}, \hat{\mathcal{L}}) = \left(\frac{-L_1 + \sqrt{L_1^2 + 4L_2L_3}}{2L_2}\right)^2 \tag{23}$$

where

$$L_1 = q + k + l\left(1 + \sum_{m=1}^{M} \frac{c_m}{g_m} + \sum_{m=1}^{M} \sqrt{\frac{\hat{\alpha} P_a d_m^2 + \sigma_m^2}{\hat{\alpha} P_a g_m^2}}\right), \tag{24}$$

$$L_2 = l \sum_{m=1}^{M} \sqrt{\frac{P_b(a_m^2 + b_m^2)}{\overline{\gamma} \hat{\alpha} P_a g_m^2}}, \tag{25}$$

$$L_3 = \sqrt{\frac{\overline{\gamma}_Y(\sigma_\zeta^2 + \sigma_Y^2)}{P_b}}. \tag{26}$$

Proof 5: See Appendix C. ■

On the other hand, the optimal value of $\overset{\star}{\alpha}$ is determined by taking the first derivative of $\alpha P_a + \beta P_b$ with respect to α and setting it to zero, i.e., $P_a + P_b \frac{d\overset{\star}{\beta}(\alpha)}{d\alpha} = 0$. Due to the complexity of this derivation, obtaining a closed-form expression is not feasible. Instead, an effective approach involves using iterative line search algorithms, such as the bisection method or the golden section method. As validated in Section VI, these numerical methods are well-suited for accurately approximating $\overset{\star}{\alpha}$ to optimize the objective function $f = -(\alpha P_a + \beta P_b)$. Finally, the optimal RIS portions for the energy efficiency regime can be computed based on the following corollary.

Corollary 2: Since the energy-efficient operation is attained when $\gamma_m = \overline{\gamma}, \forall m$, and $\gamma_Y = \overline{\gamma}_Y$, the optimal RIS partitions $\overset{\star}{\rho}_m(\overset{\star}{\alpha}, \overset{\star}{\beta}(\overset{\star}{\alpha}), \hat{\mathcal{L}})$ and $\overset{\star}{\rho}_0(\overset{\star}{\beta}(\overset{\star}{\alpha}), \hat{\mathcal{L}})$ are obtained from (17) and (18) at equality, respectively.

V. Boresight Placement Optimization

The strategic placement of beam boresights is crucial for ensuring full coverage of the PZ and optimizing overall system performance, as it directly affects both channel gains and path loss. In this section, we address the beam boresight placement problem, denoted as $\mathbf{P_o^2}$ and formulated in (15). Due to the non-convex and complex nature of $\mathbf{P_o^2}$, even small perturbations in boresight locations can lead to significant variations in the associated environmental parameters. Consequently, metaheuristic methods are particularly well-suited for performing a global search to find optimal boresight locations. Algorithm 1 demonstrates the implementation of the SA algorithm, which efficiently evaluates the fitness of candidate locations using closed-form power allocation and RIS partitioning solutions derived in the previous sections.

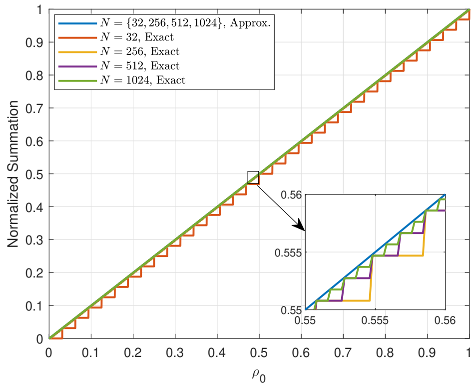

Fig. 3: The validation of approximation assumption.

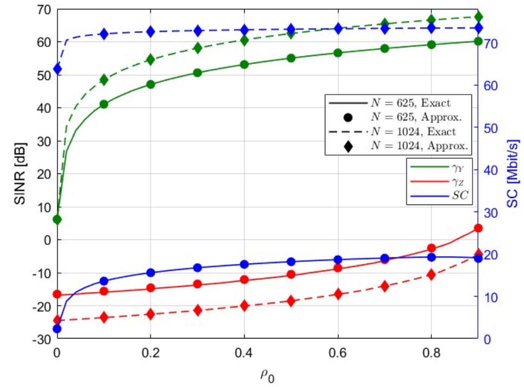

Fig. 4: The impact of ρ_0 on SINR and SC performance.

TABLE III: The Percentage of Approximation Error

N	γ_Y	γ_Z	SC
625	0.4663%	7.0797%	0.1285%
1024	0.2857%	2.4265%	0.0943%

The detailed steps of the algorithm are outlined in lines 1-18. Lines 1-6 involve inputting environmental parameters and initializing the solution. Afterward, lines 7-16 utilize procedure $\mathbf{P}_o^1$ to evaluate the fitness function by selecting new boresight locations and progressively reducing the temperature, adhering to the principles of the SA algorithm [44]. Through this iterative process, the boresight placement problem adjusts the coordinates to identify the optimal location that maximizes the objective function.

Next, we detail the power allocation and RIS partitioning procedure between lines 19-34: In line 20, the boresight locations and other environmental parameters are input, followed by the computation of optimal power allocations for Alice, $\overset{\star}{\alpha}$, and Bob, $\overset{\star}{\beta}$, in lines 21 and 22, respectively. Then, for loop in lines 23-24 determines the optimal RIS portions. Line 25 checks if the sum of the optimal RIS partition factors is less than or equal to unity. If this condition is met, the optimal objective function is computed; otherwise, the function value f is set to zero, as indicated in line 29, due to the violation of constraints. Line 27 evaluates compliance with the QoS constraints, and if these constraints are not satisfied, line 30 assigns a zero value to f. After completing these conditional checks, the optimal fitness function is finalized in line 32 and returned to SA in line 33.

VI. Simulation Results and Discussion

This section presents simulation results that analyze and demonstrate the effectiveness of the proposed scheme. The system is configured according to the network architecture illustrated in Fig. 1. The 3-D Cartesian coordinates for RIS, Alice and Bob are $(0, 0, 20), (1, 1, 20)$ and $(50 + r, 0, 0)$, respectively. The FD antennas at Alice are separated with $\lambda/2$. Moreover, micro-cell pathloss models are used as in [40]. The noise power $\sigma_x^2, \forall x \in \{Y, Z, m\}$, is calculated using Boltzmann's constant κ and the absolute temperature $T = 295K$, as $\sigma_x^2 = \kappa T \mathcal{B}$ [15]. Unless otherwise specified, the system parameters are as follows: $f_c = 4$ GHz, $\mathcal{B} = 1$ MHz, $N = 900$, $M = 4$, $r = 10$ m, $P_a = 30$ dBm, $P_b = 23$ dBm, $\eta = 0.01$, $Q_Y = 10$ Mbit/s, and $\sigma_\zeta^2 = -30$ dBm [45].

A. Comparison between Exact and Approximate Models

In this work, we assume that the RIS phase shifts are perfectly aligned with the phases of the cascaded channels, thereby eliminating the phase components and reducing the summation to involve only the channel gains. Fig. 3 presents both the exact and approximate summation expressions across different values of N, clearly demonstrating that the approximation becomes increasingly accurate as N grows. Further validation is provided in Fig. 4, which illustrates the SINR and SC results obtained from comparing the exact received signal model with the one formulated by the approximation. The approximation errors, quantified in Table III, demonstrate that the approximate SINR and SC values closely align with their exact counterparts, with relatively small deviations. Moreover, the accuracy of the approximation improves as the number of elements N increases, indicating the asymptotic tightness of the approximation. This behavior validates the use of the approximate model for the analytical formulations presented in Section II-B. Notably, the analytical results closely match the outcomes of the exact simulation, allowing us to rely on the approximate analytical results for further discussions and analysis.

B. Validation of Feasible Regime

This section provides a validation of the feasible ranges derived in Section IV-A. The analysis confirms that the conditions necessary for system performance, as established in the earlier section, are accurately represented within the derived bounds as shown in Fig. 5, wherein analytical and numerical results match tightly. Figs. 5a and 5b provide empirical validation of the analytical bounds derived in (17) and (18). As indicated in (18), ρ_0 is exclusively a function of β. Thus, an increase in β results in a decrease in ρ_0, while ρ_0 remains invariant with changes in α. In contrast, $\sum_m \rho_m$ exhibits an increasing trend with rising β and a decreasing trend with rising α as shown in (17).

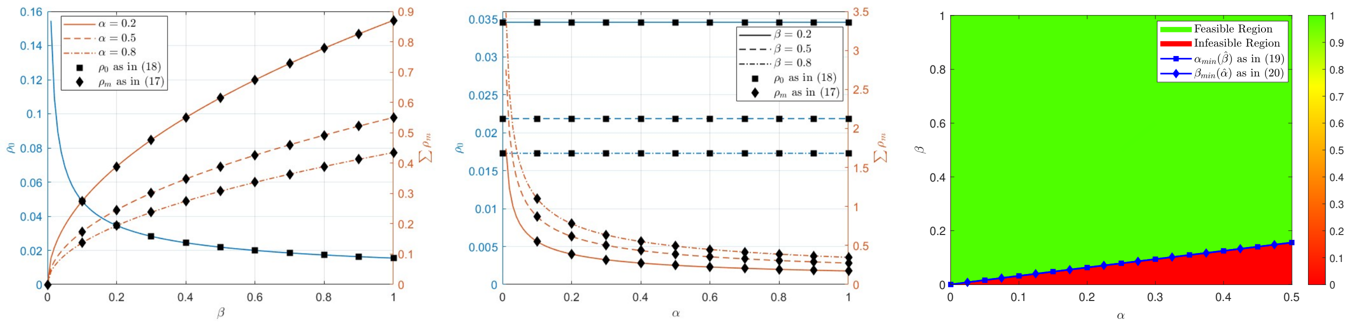

(a) (b) (c)

Fig. 5: Validation of closed-form solutions of the feasible regime: a) Optimal $\boldsymbol{\rho}$ vs. α, (b) Optimal $\boldsymbol{\rho}$ vs. β, and (c) $\alpha_{\min}$ and $\beta_{\min}$.

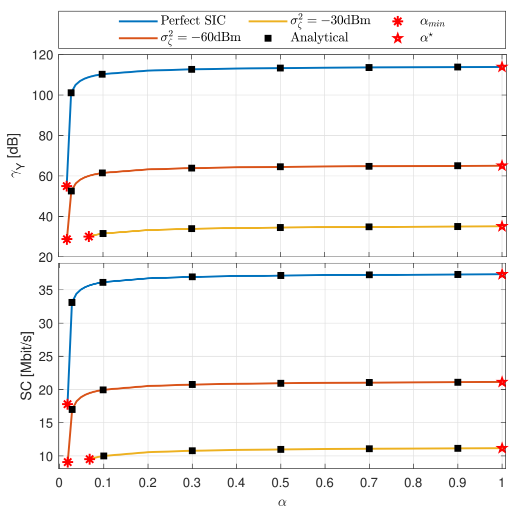

Fig. 6: The impact of AN's power on SC performance.

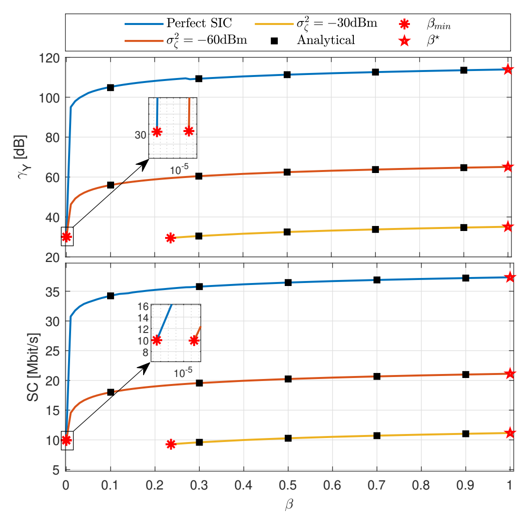

Fig. 7: The impact of Bob's power on SC performance.

Fig. 5c illustrates the feasible region where the critical constraints are satisfied: $\gamma_Y \geq \overline{\gamma}_Y$ as specified in (15b), $\gamma_m \leq \overline{\gamma}$ as defined in (15c), and $\overset{\star}{\rho}_0 + \sum_{m=1}^{M} \overset{\star}{\rho}_m \leq 1$ as required by (15d). The figure clearly delineates the boundary between feasible and infeasible regions, effectively demonstrating the system's operating limits. This boundary is precisely defined by a line, which corresponds perfectly with the theoretical constraints established by the expressions (19) and (20). This alignment between the theoretical models and the numerical results underscores the accuracy and robustness of the derived closed-forms. The feasibility region not only validates the derived limits but also offers valuable insights into the operational parameters required to maintain system stability and performance.

Moreover, the consistency between the theoretical boundaries and the observed feasible region reinforces the practical applicability of the derived closed-forms, ensuring that the system can reliably operate within these constraints in real-world scenarios. This validation is crucial for confirming that the analytical methods employed are both sound and applicable to practical implementations, providing a solid foundation for further optimization and system design.

C. Validation of Maximum SC Regime

This section presents the numerical results for $\mathbf{P_0^1}$ in the context of maximizing the SC, as discussed in Section IV-B. Figs. 6 and 7 illustrate the performance of the average SC and γ_Y under the conditions of $\hat{\beta} = 1$ and $\hat{\alpha} = 1$, respectively. These figures clearly demonstrate that the closed-form expressions for $\alpha_{\min}$ in (19) and $\beta_{\min}$ in (20) closely align with the numerical solutions, thereby validating the accuracy and reliability of the proposed analytical methods.

Figure 6 indicates that the power allocated to AN should be maximized to ensure better suppression of eavesdroppers within the PZ. Consequently, fewer RIS elements are dedicated to AN noise transmission, as reflected in equation (17). Additionally, Fig. 7 shows that the SC increases monotonically with β, indicating that maximizing Bob's power is crucial for achieving the highest γ_Y.

Furthermore, the impact of SIC on the performance of SC is examined, considering both perfect SIC scenarios with $\sigma_\zeta^2 = 0$ and imperfect SIC scenarios with $\sigma_\zeta^2 = -60$ dBm

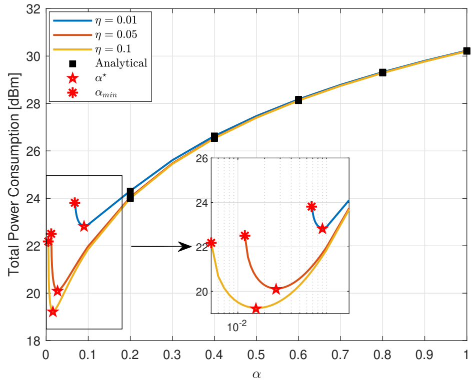

Fig. 8: The impact of AN's power on power consumption.

and $\sigma_\zeta^2 = -30$ dBm, as referenced in [45]. The results demonstrate that increased residual SI leads to a degradation in the performance of both SC and γ_Y, highlighting the critical importance of effective SIC for maintaining high spectral efficiency and optimal system performance. Quantitatively, Fig. 6 shows that an increase in σ_ζ^2 from -60 dBm to -30 dBm, with $\alpha = 0.5$, results in a degradation of SC by 16.17 Mbit/s and 26.19 Mbit/s, respectively, compared to the perfect SIC scenario. Similarly, Fig. 7 reveals a degradation in SC by 16.22 Mbit/s and 26.19 Mbit/s, respectively, under the same conditions.

D. Validation of Energy Efficiency Regime

This section presents the numerical results for $\mathbf{P_0^1}$ with $f = -(\alpha P_a + \beta P_b)$, as discussed in Section IV-C. Fig. 8 illustrates the power consumption performance as a function of α. The results demonstrate a precise alignment between the closed-form solutions and the numerical outcomes, confirming the accuracy and feasibility of the proposed method under the conditions specified in equations (19) and (20).

Moreover, Fig. 8 examines the impact of the parameter η on power consumption, where η serves as a design parameter that defines the QoS limits at $\mathcal{L}$ locations. At lower values of α, a smaller η necessitates higher power consumption, indicating that relaxing the constraint in (15c) requires increased power to effectively jam eavesdroppers across the entire PZ. Specifically, a reduction of 3.59 dBm in power consumption is observed when η is increased from 0.01 to 0.1. However, at higher values of α, the power consumption across all scenarios tends to converge closely.

E. Performance Evaluation

To evaluate the efficacy of the proposed approach, we evaluate it against the following benchmark scenarios:

- *RIS-Only:* All elements of RIS are allocated exclusively to enhance Bob's signal, with no AN transmission ($\rho_0 = 1$). This configuration is similarly studied in [8], [46]. The corresponding γ_Y and γ_Z of this approach are given by

$$\gamma_Y^{\text{RIS-Only}} = \frac{\beta P_b \left| h_{B,A} + \sum_{n=1}^{N} \boldsymbol{h_{B,R}}(n)\boldsymbol{p}(n)\boldsymbol{h_{R,A}}(n) \right|^2}{\sigma_Y^2}, \tag{27}$$

$$\gamma_Z^{\text{RIS-Only}} = \frac{\beta P_b |h_{B,E}|^2}{\sigma_Z^2}. \tag{28}$$

- *AN-Only:* Alice transmits AN to counteract Eve's reception without leveraging assistance from the RIS. This approach is similarly explored in [15], [47]. The corresponding γ_Y and γ_Z of this approach are given by

$$\gamma_Y^{\text{AN-Only}} = \frac{\beta P_b \ |h_{B,A}|^2}{\sigma_\zeta^2 + \sigma_Y^2}, \tag{29}$$

$$\gamma_Z^{\text{AN-Only}} = \frac{\beta P_b |h_{B,E}|^2}{\alpha P_a |h_{A,E}|^2 + \sigma_Z^2}. \tag{30}$$

Figure 9 presents a comprehensive performance evaluation of the aforementioned scenarios in comparison to the proposed scheme. Fig. 9a focuses on achievable capacity and SC relative to α. In the "RIS-Only" scenario, both R_Y and R_Z, as well as SC, demonstrate a lack of sensitivity to α due to the absence of AN transmission. In contrast, the "AN-Only" scenario shows that while R_Y remains constant, R_Z decreases as the AN's power increases. It is worth mentioning that the Bob-Eve channel quality surpasses that of the AN link, allowing Eve's capacity to exceed R_Y, which leads to a zero SC. The proposed scheme achieves a moderate increase in R_Y, positioned between the extremes of the "RIS-Only" and "AN-Only" scenarios. Importantly, the proposed scheme significantly limits Eve's capacity, thus minimizing the leakage of confidential information. In terms of SC, the proposed scheme demonstrates superior performance by strategically allocating more RIS elements to beams directed towards Bob's location, thereby enhancing the protection against potential eavesdroppers.

Figure 9b illustrates the impact of the number of RIS elements on the different scenarios discussed above. In the "RIS-Only" scenario, where all RIS elements are allocated to Bob's transmission, it is observed that R_Y increases with the number of elements N, while R_Z remains constant and lower than R_Y. This results in a non-negative SC that increases as N grows. In contrast, the "AN-Only" scenario, in which the RIS is not part of the network, shows no changes in R_Y and R_Z with increasing N. However, this approach results in a zero secrecy capacity, as R_Z exceeds R_Y. The proposed scheme demonstrates that increasing the number of RIS elements leads to more elements being allocated to Bob's transmission, which is clearly reflected in the enhancement of R_Y as N increases. This, in turn, significantly improves the overall security level.

Figure 9c illustrates the impact of FD capability on the SC performance of the scenarios discussed earlier, with a particular focus on the effect of residual SI power, σ_ζ^2. As shown, σ_ζ^2 and P_a have no impact on the SC in the "RIS-Only" scenario, as no IBFD system is involved. However, consistent

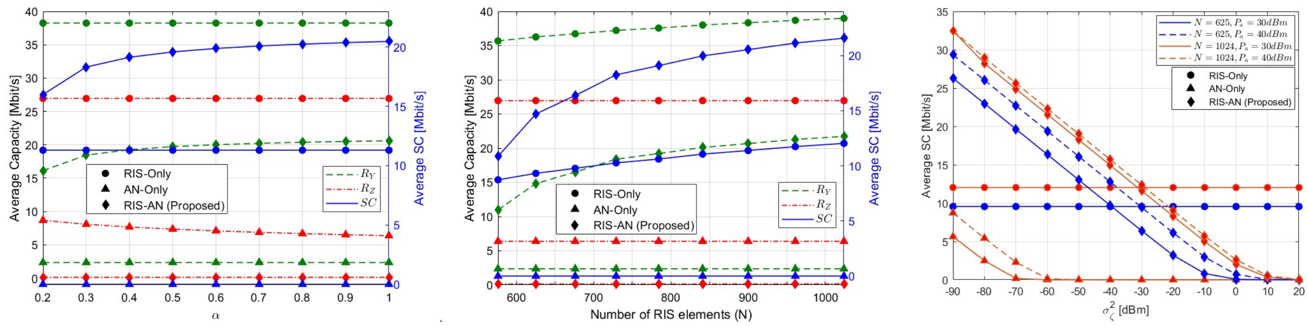

(a) (b) (c)

Fig. 9: Performance evaluation of the proposed scheme in terms of: (a) AN power allocation factor, (b) Number of RIS elements, and (c) Residual SI power.

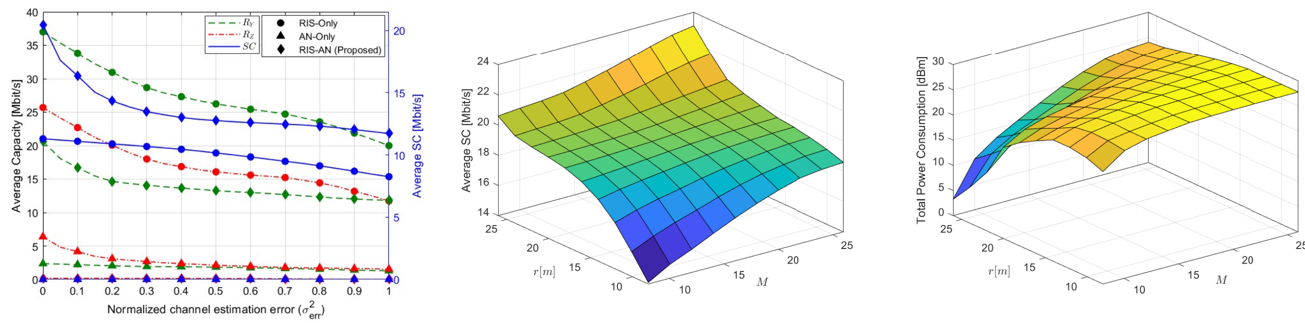

(a) (b) (c)

Fig. 10: Performance evaluation of the proposed scheme considering: (a) the effect of channel estimation errors, (b) the impact of radius and the number of beams on SC, and (c) the impact of radius and the number of beams on power consumption.

with the results in Fig. 9b, the SC in the "RIS-Only" scenario improves with an increase in the number of RIS elements. Fig. 9c also highlights the sensitivity of the SC in the "AN-Only" scenario to SIC. The "AN-Only" scenario can tolerate residual SI levels up to approximately -70 dBm. Nevertheless, the SC performance of the "AN-Only" scenario remains inferior to that of the "RIS-Only" scenario. It is evident that increasing the power allocated to AN improves the SC performance and reduces sensitivity to SIC. The proposed scheme demonstrates lower sensitivity to SIC compared to the "AN-Only" scenario, being capable of handling residual SI levels up to 0 dBm. Moreover, the proposed scheme outperforms the "RIS-Only" approach when σ_ζ^2 is less than -40 dBm. However, in cases of bad SIC techniques, the "RIS-Only" approach is preferable. The results also indicate that increasing the power of AN further reduces the proposed scheme's sensitivity to SIC. Specifically, increasing P_a from 30 dBm to 40 dBm lowers the threshold of σ_ζ^2 from -40 dBm to -30 dBm, allowing the proposed scheme to outperform the other scenarios discussed. Additionally, it is shown that increasing AN's power leads to a slight increase in SC as the size of the RIS increases.

Since the proposed scheme relies on CSI, its performance is susceptible to degradation due to channel estimation errors. Fig. 10a evaluates the robustness of the proposed scheme and previously discussed scenarios under imperfect channel conditions[11]. The channel estimation model is expressed as $h_{u,v}^{est} = h_{u,v} + \epsilon$, where $h_{u,v}^{est}$ represents the estimated channel, and $\epsilon \sim \mathcal{CN}(0, \sigma_{err}^2)$ denotes the channel estimation error. The error follows a circularly symmetric complex Gaussian distribution with zero mean and variance σ_{err}^2. Generally, both the achievable capacity and SC degrade as σ_{err}^2 increases. Compared to the case of perfect CSI (i.e., $\sigma_{err}^2 = 0$), the proposed scheme exhibits a SC loss of less than 4.1 Mbit/s when $\sigma_{err}^2 = 0.1$. However, in the "RIS-Only" scenario, the SC loss is significantly lower, approximately 0.2 Mbit/s. Despite this degradation, the trade-off is necessary to ensure a higher security level in the system. Specifically, with $\sigma_{err}^2 = 0.1$, the proposed scheme achieves a SC of approximately 16.4 Mbit/s, whereas the "RIS-Only" approach attains only 11.1 Mbit/s.

Although the proposed approach demonstrates robust performance compared to the benchmark scenarios, it relies on the availability of full instantaneous CSI, which imposes significant channel estimation overhead, particularly in dynamic channel environments. A more practical alternative to mitigate this challenge involves the use of RIS beam training or codebook-based methods [48], enabling flexible selection and subsampling of beams to effectively manage overhead. Incorporating such low-overhead RIS configuration techniques into the current framework represents a promising and necessary

[11] We also account for imperfections in the geometric channel model used to characterize the channel between RIS to ℓ_m.

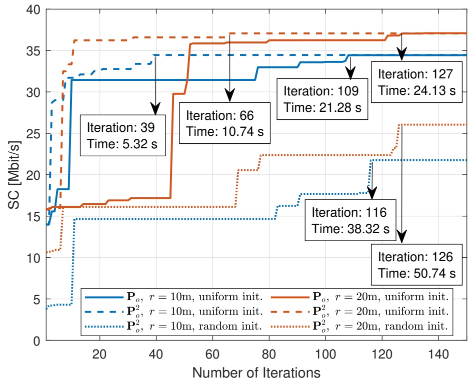

Fig. 11: The convergence performance for maximum SC regime.

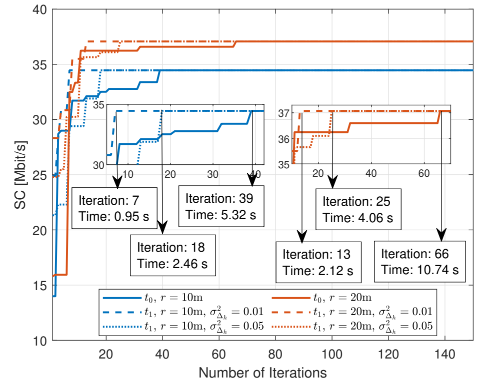

Fig. 12: The impact of channel variations on the convergence performance.

avenue for future research, which will be essential for enabling scalable and efficient RIS-assisted communication systems in realistic deployment scenarios.

Figures 10b and 10c analyze the impact of the PZ radius and the number of beams on SC and power consumption, respectively. Here, Bob's location is fixed at the coordinates $(60, 0, 0)$. As shown in Fig. 10b, doubling the radius from $r = 10$m to $r = 20$m results in an increase in SC of approximately 3.7 Mbit/s. Similarly, increasing the number of beams from $M = 10$ to $M = 16$ enhances SC by approximately 1.9 Mbit/s. These results indicate that increasing either the radius or the number of beams contributes to an improvement in SC. In terms of power consumption, increasing the PZ radius leads to a reduction in power consumption, as depicted in Fig. 10c. Specifically, doubling the radius from $r = 10$m to $r = 20$m results in a power consumption decrease of approximately 5.6 dBm. Conversely, a higher number of beams increases power consumption due to the additional processing and transmission overhead. For instance, employing 10 beams requires approximately 25.5 dBm, whereas increasing the number of beams to 16 raises the power consumption to approximately 27.5 dBm. These findings highlight the trade-off between SC enhancement and power efficiency when adjusting the system parameters.

F. Time Complexity and Convergence Analysis

This section presents the time complexity and convergence behavior of $\mathbf{P_o^2}$ using the SA approach, as discussed in Section V. Fig. 11 illustrates the convergence in the maximum SC regime. Therefore, Fig. 11 compares the convergence behavior when optimizing all parameters using the SA approach, as in $\mathbf{P_o}$, with optimizing only the boresight locations as in $\mathbf{P_o^2}$. The analysis is conducted for two PZ sizes: $r = 10$ m and $r = 20$ m. The results indicate that the convergence of $\mathbf{P_o^2}$ is approximately 1.2 times faster than that of $\mathbf{P_o}$, which can be attributed to the efficiency of the closed-form solutions.. Notably, the convergence rates in both cases are highly efficient. For example, when $r = 20$ m, $\mathbf{P_o^2}$ converges within 66 iterations over 10.74 seconds, whereas $\mathbf{P_o}$ converges after 127 iterations, taking 24.13 seconds. Additionally, the convergence time decreases for both cases as the PZ size is reduced. Specifically, the convergence time of $\mathbf{P_o^2}$ is halved when $r = 10$ m compared to $r = 20$ m. Similarly, for $\mathbf{P_o}$, the convergence time decreases by approximately 3 seconds with $r = 10$ m compared to $r = 20$ m.

Additionally, the impact of the initial boresight locations on system performance is examined. Fig. 11 illustrates two boresight initialization strategies: *uniform*, where the boresight locations are evenly distributed along the y-axis, and *random*, where the boresight locations are distributed randomly along the y-axis. As shown, different initializations result in variations in the convergence behavior and the achievable SC. For instance, with a random initialization at $r = 10$m, the algorithm converges within 116 iterations, achieving an SC of 21.75 Mbit/s, whereas uniform initialization results in a faster convergence within 39 iterations and a higher SC of 34.46 Mbit/s.

The impact of channel variations on convergence performance is analyzed in Fig. 12. In this analysis, we assume that at time instance t_0, the channels are represented by h, whereas at time instance t_1, the channels are given by $h + \delta_h$, where $\delta_h \sim \mathcal{CN}(0, \sigma^2_{\Delta_h})$ denotes the channel variation. Additionally, at t_1, the boresight locations are initialized using the optimized boresight locations from t_0. As observed in Fig. 12, at t_0, the algorithm converges within 39 iterations, requiring approximately 5.32 seconds when the PZ radius is 10m. However, at t_1 when the channel variation follows $\sigma^2_{\Delta_h} = 0.05$, the algorithm achieves convergence in 18 iterations, requiring 2.46 seconds. For smaller channel variations ($\sigma^2_{\Delta_h} = 0.01$), the algorithm converges even faster, completing within 7 iterations in just 0.95 seconds. A similar trend is observed when the PZ radius is increased to 20m, demonstrating that larger channel variations lead to slower convergence, whereas smaller variations significantly enhance convergence speed. In conclusion, these results validate the efficiency of our proposed approach in handling mobile communication systems.

VII. Conclusion and Future Directions

This study introduces a novel RIS-aided AN scheme for FD networks aimed at enhancing wireless security. By leveraging

FD capabilities and strategic RIS partitioning, the proposed scheme not only strengthens secure transmissions between legitimate entities but also actively disrupts passive eavesdroppers. The effectiveness of the scheme is evaluated in terms of (a) secrecy capacity and (b) power consumption. Closed-form solutions for the optimal allocation of RIS elements and transmit power for both Alice and Bob are derived. The results indicate that the derived closed-form solutions align perfectly with numerical results. Additionally, the boresight placement is optimized using a SA algorithm to address the significant environmental changes caused by minor location adjustments. This comprehensive approach demonstrates the potential for significant improvements in both security and efficiency in wireless systems.

As part of future work, a key direction involves extending the proposed framework to practical channel environments, such as frequency-selective channels and multi-carrier systems, which are common in modern broadband networks. These scenarios require more sophisticated RIS phase shift strategies to address time and frequency variations. Additionally, to reduce the reliance on full instantaneous CSI, integrating low-overhead RIS configuration techniques, such as beam training or codebook-based methods, offers a promising path toward practical implementation. These extensions are essential for enhancing the real-world applicability of the proposed scheme.

Acknowledgment

This research is supported by The Scientific and Technological Research Council of Türkiye (TÜBİTAK) under Grant Number 123E226, and partially funded by the Science Committee of the Ministry of Science and Higher Education of the Republic of Kazakhstan under Grant Number AP22788920.

Appendix A
Proof of Feasible Regime

To determine the feasible range for ρ_m for fixed boresight locations, it is essential to satisfy the constraint $\gamma_m(\hat{\alpha}, \hat{\beta}, \boldsymbol{\rho}, \hat{\boldsymbol{\mathcal{L}}}) \leq \overline{\gamma}$, where γ_m in (13) can be rewritten by introducing the channel coefficients $h_{B,m} = a_m + \jmath b_m$, $h_{A,m} = c_m + \jmath d_m$ and $\sum_{n=1}^{N} \boldsymbol{h_{A,R}}(n)\boldsymbol{p}(n)\boldsymbol{h_{R,m}}(n) = g_m$. This yields to the following expression

$$\frac{\hat{\beta} P_b(a_m^2 + b_m^2)}{\hat{\alpha} P_a((c_m + \rho_m f_m)^2 + d_m^2) + \sigma_m^2} \leq \overline{\gamma}. \tag{A.1}$$

By isolating ρ_m, the feasible range for AN's RIS portion factor is derived as

$$\overset{\star}{\rho}_m(\hat{\alpha}, \hat{\beta}, \hat{\boldsymbol{\mathcal{L}}}) \geq \frac{-c_m + \sqrt{\frac{\hat{\beta} P_b(a_m^2+b_m^2)}{\hat{\alpha} P_a \overline{\gamma}} - \frac{\sigma_m^2}{\hat{\alpha} P_a} - d_m^2}}{g_m}. \tag{A.2}$$

Next, by considering the second condition where $\gamma_Y(\hat{\beta}, \boldsymbol{\rho}, \hat{\boldsymbol{\mathcal{L}}}) \geq \overline{\gamma}_Y$, where γ_Y, from (9) can be re-expressed by introducing the channel coefficient as $h_{B,A} = q + \jmath k$ and $\sum_{n=1}^{N} \boldsymbol{h_{B,R}}(n)\boldsymbol{p}(n)\boldsymbol{h_{R,A}}(n) = l$. This yields to

$$\frac{\hat{\beta} P_b((q + \rho_0 l)^2 + k^2)}{\sigma_\zeta^2 + \sigma_Y^2} \geq \overline{\gamma}_Y \tag{A.3}$$

Solving for ρ_0 yields the following expression for the feasible range of the RIS partition factor associated with legitimate transmission

$$\overset{\star}{\rho}_0(\hat{\beta}, \hat{\boldsymbol{\mathcal{L}}}) \geq -\frac{q}{l} + \sqrt{\frac{\overline{\gamma}_Y(\sigma_\zeta^2 + \sigma_Y^2) - \beta P_b k^2}{\beta P_b l^2}}. \tag{A.4}$$

The validity of both (A.2) and (A.4) is contingent upon the condition that the sum of all RIS partition factors does not exceed unity, resulting in the constraint

$$\overset{\star}{\rho}_0(\beta, \hat{\boldsymbol{\mathcal{L}}}) + \sum_{m=1}^{M} \overset{\star}{\rho}_m(\alpha, \beta, \hat{\boldsymbol{\mathcal{L}}}) \leq 1 \tag{A.5}$$

By solving (A.5) for α and applying the upper-bound of inequality $\sqrt{\mathcal{X} \pm \mathcal{Y}} \leq \sqrt{\mathcal{X}} \pm \sqrt{\mathcal{Y}}$, the feasible range for the AN power allocation factor, for given $\hat{\beta}$, is obtained as follows

$$\alpha(\hat{\beta}) \geq \left(\frac{\sum_{m=1}^{M} \sqrt{\frac{\hat{\beta} P_b(a_m^2+b_m^2) - \overline{\gamma}\sigma_m^2}{\overline{\gamma} P_a g_m^2}}}{1 + \frac{q}{l} + \sum_{m=1}^{M} \frac{d_m + c_m}{g_m} - \sqrt{\frac{\overline{\gamma}_Y(\sigma_\zeta^2+\sigma_Y^2) - \hat{\beta} P_b k^2}{\hat{\beta} P_b l^2}}} \right)^2. \tag{A.6}$$

In this context, $\alpha_{\min}$ is defined as the lower bound of (A.6) and can be written as in (19).

Likewise, the feasible range for Bob's power allocation factor by solving (A.5) for β, which is expressed, for a given $\hat{\alpha}$, as follows

$$\beta(\hat{\alpha}) \geq \left(\frac{-\Lambda + \sqrt{\Lambda^2 - 4\sqrt{\frac{\overline{\gamma}_Y(\sigma_\zeta^2+\sigma_Y^2)}{P_b l^2}} \sum_{m=1}^{M} \sqrt{\frac{u_m}{g_m^2}}}}{2\sum_{m=1}^{M} \sqrt{\frac{u_m}{g_m^2}}} \right)^2. \tag{A.7}$$

Here, $\Lambda = 1 + \frac{q+k}{l} + \sum_{m=1}^{M} \frac{c_m + d_m}{g_m} + \sum_{m=1}^{M} \sqrt{\frac{\sigma_m^2}{\hat{\alpha} P_a g_m^2}}$, and $u_m = \frac{P_b(a_m^2+b_m^2)}{\overline{\gamma}\hat{\alpha} P_a}$. Consequently, $\beta_{\min}$ represents the minimum value that satisfies (A.7) and can be written as in (20). ■

Appendix B
Proof of Maximum SC Regime

To determine that $\gamma_{SC}(\alpha, \beta, \boldsymbol{\rho}, \hat{\boldsymbol{\mathcal{L}}})$ is non-negative, it is necessary to show that $\gamma_Y(\beta, \boldsymbol{\rho}, \hat{\boldsymbol{\mathcal{L}}})$ exhibits a monotonic increase with respect to β at a rate faster than $\gamma_m(\alpha, \beta, \boldsymbol{\rho}, \hat{\boldsymbol{\mathcal{L}}})$. This condition is satisfied when the inequality $\frac{\mathrm{d}\gamma_Y}{\mathrm{d}\beta} > \frac{\mathrm{d}\gamma_m}{\mathrm{d}\beta}$ holds, which can be expressed as

$$\frac{P_b((q + \rho_0 l)^2 + k^2)}{\sigma_\zeta^2 + \sigma_Y^2} > \frac{P_b(a_m^2 + b_m^2)}{\alpha P_a((c_m + \rho_m g_m)^2 + d_m^2) + \sigma_m^2}. \tag{B.1}$$

Within this context, the feasibility conditions are established by ensuring that $\gamma_Y \geq \overline{\gamma}_Y$ and $\gamma_m \leq \overline{\gamma}$, where by definition $\overline{\gamma}_Y \ggg \overline{\gamma}$. This relationship can be succinctly expressed as

$$\beta \cdot \mathrm{LHS} = \gamma_Y \geq \overline{\gamma}_Y \ggg \overline{\gamma} \geq \gamma_m = \beta \cdot \mathrm{RHS}, \tag{B.2}$$

where LHS and RHS denote the left-hand side and right-hand side of (B.1), respectively. We can deduce from (B.2) that the condition in (B.1) always holds, thereby allowing us to conclude that $\gamma_Y(\beta, \boldsymbol{\rho}, \hat{\boldsymbol{\mathcal{L}}})$ increases monotonically at a rate faster than $\gamma_m(\alpha, \beta, \boldsymbol{\rho}, \hat{\boldsymbol{\mathcal{L}}})$ w.r.t. β. As a result, the optimal value $\overset{\star}{\beta}$ corresponds to the maximum within the range of β, specifically $\beta \in [0, 1]$. Therefore, the optimal value of $\overset{\star}{\beta}$ is determined to be 1.

Appendix C
Proof of Energy Efficiency Regime

To find the optimal Bob's power allocation factor, $\overset{\star}{\beta}$, that minimizes the power consumption, we proceed as follows. Firstly, the RIS elements must be fully exploited; i.e, $\overset{\star}{\rho}_0(\beta, \hat{\boldsymbol{\mathcal{L}}}) + \sum_{m=1}^{M} \overset{\star}{\rho}_m(\alpha, \beta, \hat{\boldsymbol{\mathcal{L}}}) = 1$, where $\overset{\star}{\rho}_0(\beta, \hat{\boldsymbol{\mathcal{L}}})$ and $\overset{\star}{\rho}_m(\alpha, \beta, \hat{\boldsymbol{\mathcal{L}}})$ are defined in (A.4) and (A.2), respectively. By further simplifying the expression, we obtain the following

$$lC_2\beta + (h + lC_1 + k)\sqrt{\beta} - \sqrt{\frac{\overline{\gamma}_Y(\sigma_\zeta^2 + \sigma_Y^2)}{P_b}} = 0, \tag{C.1}$$

where

$$C_1 = 1 + \sum_{m=1}^{M} \frac{c_m}{g_m} + \sum_{m=1}^{M} \sqrt{\frac{\alpha P_a d_m^2 + \sigma_m^2}{\alpha P_a g_m^2}} \tag{C.2}$$

and

$$C_2 = \sum_{m=1}^{M} \sqrt{\frac{P_b(a_m^2 + b_m^2)}{\overline{\gamma}\alpha P_a g_m^2}}. \tag{C.3}$$

By solving for β, the optimal $\overset{\star}{\beta}$ can be written as in (23). ■

References

[1] Z. Zhang *et al.*, “6G wireless networks: Vision, requirements, architecture, and key technologies,” *IEEE Veh. Technol. Mag.*, vol. 14, no. 3, pp. 28–41, 2019.

[2] K. B. Letaief, W. Chen, Y. Shi, J. Zhang, and Y.-J. A. Zhang, “The roadmap to 6G: AI empowered wireless networks,” *IEEE Commun. Mag.*, vol. 57, no. 8, pp. 84–90, 2019.

[3] C.-X. Wang *et al.*, “On the road to 6G: Visions, requirements, key technologies and testbeds,” *IEEE Commun. Surv. Tutor.*, vol. 25, no. 2, pp. 905–974, 2023.

[4] Y. Zou, “Intelligent interference exploitation for heterogeneous cellular networks against eavesdropping,” *IEEE J. Sel. Areas Commun.*, vol. 36, no. 7, pp. 1453–1464, 2018.

[5] M. S. J. Solaija, H. Salman, and H. Arslan, “Towards a Unified Framework for Physical Layer Security in 5G and Beyond Networks,” *IEEE Open J. Veh. Technol.*, vol. 3, pp. 321–343, 2022.

[6] A. Celik and A. M. Eltawil, “At the Dawn of Generative AI Era: A tutorial-cum-survey on new frontiers in 6G wireless intelligence,” *IEEE Open J. Commun. Soc.*, 2024.

[7] J. M. Hamamreh, H. M. Furqan, and H. Arslan, “Classifications and applications of physical layer security techniques for confidentiality: A comprehensive survey,” *IEEE Commun. Surv. Tutor.*, vol. 21, no. 2, pp. 1773–1828, 2018.

[8] G. Zhou, C. Pan, H. Ren, K. Wang, and Z. Peng, “Secure Wireless Communication in RIS-Aided MISO System With Hardware Impairments,” *IEEE Wirel. Commun. Lett.*, vol. 10, no. 6, pp. 1309–1313, 2021.

[9] Y. Chen *et al.*, “Next-Generation Full Duplex Networking Systems Empowered by Reconfigurable Intelligent Surfaces,” *IEEE Trans. Wirel. Commun.*, 2023.

[10] S. Goel and R. Negi, “Guaranteeing secrecy using artificial noise,” *IEEE Trans. Wirel. Commun.*, vol. 7, no. 6, pp. 2180–2189, 2008.

[11] J. Zhu, R. Schober, and V. K. Bhargava, “Secure transmission in multicell massive MIMO systems,” *IEEE Trans. Wirel. Commun.*, vol. 13, no. 9, pp. 4766–4781, 2014.

[12] Z. Li, W. Trappe, and R. Yates, “Secret communication via multi-antenna transmission,” in *IEEE Annu. Conf. Inf. Sci. Syst.*, 2007, pp. 905–910.

[13] L. Mucchi, S. Caputo, P. Marcocci, G. Chisci, L. Ronga, and E. Panayirci, “Security and reliability performance of noise-loop modulation: Theoretical analysis and experimentation,” *IEEE Trans. Veh. Technol.*, vol. 71, no. 6, pp. 6335–6350, 2022.

[14] W. Li, M. Ghogho, B. Chen, and C. Xiong, “Secure communication via sending artificial noise by the receiver: Outage secrecy capacity/region analysis,” *IEEE Commun. Lett.*, vol. 16, no. 10, pp. 1628–1631, 2012.

[15] X. Guan, Q. Wu, and R. Zhang, “Intelligent reflecting surface assisted secrecy communication: Is artificial noise helpful or not?” *IEEE Wirel. Commun. Lett.*, vol. 9, no. 6, pp. 778–782, 2020.

[16] W. Long, R. Chen, M. Moretti, W. Zhang, and J. Li, “A promising technology for 6G wireless networks: Intelligent reflecting surface,” *J. Commun. Inf. Netw.*, vol. 6, no. 1, pp. 1–16, 2021.

[17] Y.-C. Liang, R. Long, Q. Zhang, J. Chen, H. V. Cheng, and H. Guo, “Large intelligent surface/antennas (LISA): Making reflective radios smart,” *J. Commun. Inf. Netw.*, vol. 4, no. 2, pp. 40–50, 2019.

[18] H. Yang, Z. Xiong, J. Zhao, D. Niyato, Q. Wu, H. V. Poor, and M. Tornatore, “Intelligent reflecting surface assisted anti-jamming communications: A fast reinforcement learning approach,” *IEEE Trans. Wirel. Commun.*, vol. 20, no. 3, pp. 1963–1974, 2020.

[19] H. Shen, W. Xu, S. Gong, Z. He, and C. Zhao, “Secrecy rate maximization for intelligent reflecting surface assisted multi-antenna communications,” *IEEE Commun. Lett.*, vol. 23, no. 9, pp. 1488–1492, 2019.

[20] H.-M. Wang, J. Bai, and L. Dong, “Intelligent reflecting surfaces assisted secure transmission without eavesdropper's CSI,” *IEEE Signal Process. Lett.*, vol. 27, pp. 1300–1304, 2020.

[21] L. Yang, J. Yang, W. Xie, M. O. Hasna, T. Tsiftsis, and M. Di Renzo, “Secrecy performance analysis of RIS-aided wireless communication systems,” *IEEE Trans. Veh. Technol.*, vol. 69, no. 10, pp. 12 296–12 300, 2020.

[22] A. Almohamad, A. M. Tahir, A. Al-Kababji, H. M. Furqan, T. Khattab, M. O. Hasna, and H. Arslan, “Smart and secure wireless communications via reflecting intelligent surfaces: A short survey,” *IEEE Open J. Commun.*, 2020.

[23] F. Naeem, M. Ali, G. Kaddoum, C. Huang, and C. Yuen, “Security and privacy for reconfigurable intelligent surface in 6G: A review of prospective applications and challenges,” *IEEE Open J. Commun.*, 2023.

[24] D. Nguyen, L.-N. Tran, P. Pirinen, and M. Latva-aho, “On the spectral efficiency of full-duplex small cell wireless systems,” *IEEE Trans. Wirel. Commun.*, vol. 13, no. 9, pp. 4896–4910, 2014.

[25] M. Duarte and A. Sabharwal, “Full-duplex wireless communications using off-the-shelf radios: Feasibility and first results,” in *IEEE Conf. Rec. 44th Asilomar Conf. Signals, Syst. Comput.*, 2010, pp. 1558–1562.

[26] H. Shen, T. Ding, W. Xu, and C. Zhao, “Beamforming design with fast convergence for IRS-aided full-duplex communication,” *IEEE Commun. Lett.*, vol. 24, no. 12, pp. 2849–2853, 2020.

[27] Y. Cai, M.-M. Zhao, K. Xu, and R. Zhang, “Intelligent reflecting surface aided full-duplex communication: Passive beamforming and deployment design,” *IEEE Trans. Wirel. Commun.*, vol. 21, no. 1, pp. 383–397, 2021.

[28] Z. Peng, Z. Zhang, L. Kong, C. Pan, L. Li, and J. Wang, “Deep reinforcement learning for RIS-aided multiuser full-duplex secure communications with hardware impairments,” *IEEE Internet Things J.*, vol. 9, no. 21, pp. 21 121–21 135, 2022.

[29] P. Guan, Y. Wang, and Y. Zhao, “Secure Wireless Transmission for Reconfigurable Intelligent Surface Aided Full Duplex Systems,” *arXiv preprint arXiv:2206.08797*, 2022.

[30] S. Arzykulov, A. Celik, G. Nauryzbayev, and A. M. Eltawil, “Artificial noise and RIS-aided physical layer security: Optimal RIS partitioning and power control,” *IEEE Wirel. Commun. Lett.*, vol. 12, no. 6, pp. 992–996, 2023.

[31] N. Romero-Zurita, D. McLernon, M. Ghogho, and A. Swami, “PHY layer security based on protected zone and artificial noise,” *IEEE Signal Process. Lett.*, vol. 20, no. 5, pp. 487–490, 2013.

[32] X. Ji, X. Kang, K. Huang, N. Li, and M. Yi, “The full-duplex artificial noise scheme for security of a cellular system,” *China Commun.*, vol. 12, no. Supplement, pp. 150–156, 2015.

[33] S. Arzykulov, A. Celik, G. Nauryzbayev, and A. M. Eltawil, “Aerial ris-aided physical layer security: Optimal deployment and partitioning,” *IEEE Trans. Cogn. Commun. Netw.*, 2024.

[34] G. Zheng, I. Krikidis, J. Li, A. P. Petropulu, and B. Ottersten, “Improving physical layer secrecy using full-duplex jamming receivers,” *IEEE Trans. Signal Process.*, vol. 61, no. 20, pp. 4962–4974, 2013.

[35] Y. S. Cho, J. Kim, W. Y. Yang, and C. G. Kang, *MIMO-OFDM wireless communications with MATLAB*. John Wiley & Sons, 2010.

[36] X. Hu, C. Zhong, Y. Zhang, X. Chen, and Z. Zhang, "Location Information Aided Multiple Intelligent Reflecting Surface Systems," *IEEE Trans. Commun.*, vol. 68, no. 12, pp. 7948–7962, 2020.

[37] H. Lee, S. Kim, and J. Choi, "Efficient channel AoD/AoA estimation using widebeams for millimeter wave MIMO systems," in *IEEE 20th Int. Workshop Signal Process. Adv. Wireless Commun. (SPAWC)*, 2019, pp. 1–5.

[38] J. Luo, F. Wang, S. Wang, H. Wang, and D. Wang, "Reconfigurable intelligent surface: Reflection design against passive eavesdropping," *IEEE Trans. Wirel. Commun.*, vol. 20, no. 5, pp. 3350–3364, 2021.

[39] Z. Xing, R. Wang, J. Wu, and E. Liu, "Achievable rate analysis and phase shift optimization on intelligent reflecting surface with hardware impairments," *IEEE Trans. Wirel. Commun.*, vol. 20, no. 9, pp. 5514–5530, 2021.

[40] E. Björnson, H. Wymeersch, B. Matthiesen, P. Popovski, L. Sanguinetti, and E. de Carvalho, "Reconfigurable intelligent surfaces: A signal processing perspective with wireless applications," *IEEE Signal Process. Mag.*, vol. 39, no. 2, pp. 135–158, 2022.

[41] E. Björnson and L. Sanguinetti, "Rayleigh fading modeling and channel hardening for reconfigurable intelligent surfaces," *IEEE Wirel. Commun. Lett.*, vol. 10, no. 4, pp. 830–834, 2020.

[42] S. Boyd and L. Vandenberghe, *Convex optimization*. Cambridge university press, 2004.

[43] W. Lv, J. Bai, Q. Yan, and H. M. Wang, "RIS-Assisted Green Secure Communications: Active RIS or Passive RIS?" *IEEE Wirel. Commun. Lett.*, vol. 12, no. 2, pp. 237–241, 2023.

[44] Y. Eren, İbrahim B. Küçükdemiral, and İlker Üstoğlu, "Chapter 2 - Introduction to Optimization," in *Optimization in Renewable Energy Systems*. Boston: Butterworth-Heinemann, 2017, pp. 27–74.

[45] B. Yu, C. Qian, P. Lin, S. Shao, W. Pan, Y. Shen, S. Hu, D. Su, C. Sun, Q. Xiong *et al.*, "Full duplex communication with practical self-interference cancellation implementation," in *IEEE Int. Conf. Commun. (ICC)*. IEEE, 2022, pp. 1100–1105.

[46] J. Qiao and M.-S. Alouini, "Secure Transmission for Intelligent Reflecting Surface-Assisted mmWave and Terahertz Systems," *IEEE Wirel. Commun. Lett.*, vol. 9, no. 10, pp. 1743–1747, 2020.

[47] B. Feng, Y. Wu, M. Zheng, X.-G. Xia, Y. Wang, and C. Xiao, "Large intelligent surface aided physical layer security transmission," *IEEE Trans. Signal Process.*, vol. 68, pp. 5276–5291, 2020.

[48] X. Wei, L. Dai, Y. Zhao, G. Yu, and X. Duan, "Codebook design and beam training for extremely large-scale RIS: Far-field or near-field?" *China Commun.*, vol. 19, no. 6, pp. 193–204, 2022.

Hanadi Salman (Graduate Student Member, IEEE) received the B.S. degree (Hons.) in Telecommunication Engineering from An-Najah National University, Palestine, in 2017. She is currently pursuing the Ph.D. degree with Istanbul Medipol University, Türkiye, where she is also a Research Assistant with the Communications, Signal Processing, and Networking Center (CoSiNC). Her research interests include interference management, full-duplex communications, and coordinated multi-point techniques, with a focus on secure and efficient wireless communication systems for beyond-5G and 6G networks.

Abdulkadir Celik (Senior Member, IEEE) is an associate professor and the Head of the Centre for Internet of Things and Pervasive Systems in the School of Electronics and Computer Science at the University of Southampton. He received the Ph.D. degree in co-majors of Electrical Engineering and Computer Engineering from Iowa State University, Ames, IA, USA, in 2016; wherein he also earned M.S. degrees in Electrical Engineering and Computer Engineering in 2013 and 2015, respectively. Prior to his current appointment, he was a senior research scientist from 2020 to 2025 and a post-doctoral fellow from 2016 to 2020 at King Abdullah University of Science and Technology (KAUST), Thuwal, KSA. Dr. Çelik is the recipient of IEEE Communications Society's 2023 Outstanding Young Researcher Award for Europe, Middle East, and Africa (EMEA) region. He currently serves as an editor for `npj` Wireless Technology, IEEE Transactions on Communications, IEEE Communications Letters, IEEE Wireless Communication Letters, and Frontiers in Communications and Networks. His research interests are in the broad areas of next-generation wireless communication systems and networks.

Sultangali Arzykulov (Senior Member, IEEE) received the B.Sc. degree (Hons.) in radio engineering, electronics, and telecommunications from Kazakh National Research Technical University, Almaty, Kazakhstan, in 2010, the M.Sc. degree in communication engineering from the University of Manchester, Manchester, U.K., in 2013, and the Ph.D. degree in science, engineering, and technology from Nazarbayev University, Nur-Sultan, Kazakhstan, in 2019. He has served as a Postdoctoral Scholar with Nazarbayev University from 2019 to 2020 and as a Postdoctoral Fellow with the King Abdullah University of Science and Technology, Saudi Arabia, from 2020 to 2023. In 2023, he joined Nazarbayev University as an Assistant Professor. His research interests are centered around wireless communication systems, specifically focusing on intelligent reconfigurable surfaces, cognitive radio, energy harvesting, interference mitigation in full-duplex systems, and non-orthogonal multiple access. His academic career is distinguished by his roles as a reviewer and a technical program committee member for several international journals and the IEEE Communications Society flagship conferences.

Ahmed M. Eltawil (Senior Member, IEEE) is a Professor and Associate Dean for Research at the Computer, Electrical, and Mathematical Sciences and Engineering (CEMSE) Division at King Abdullah University of Science and Technology (KAUST). Previously, he was a Professor of Electrical Engineering and Computer Science at the University of California, Irvine (UCI) from 2005 to 2021. Professor Eltawil earned his doctorate degree from the University of California, Los Angeles, in 2003 and his Master's and Bachelor's degrees from Cairo University in 1999 and 1997, respectively. At KAUST, he established the Communication and Computing Systems Laboratory (CCSL) to conduct research on efficient architectures for computing and communications systems, with a particular focus on mobile wireless systems. His research interests encompass various application domains, such as low-power mobile systems, machine learning platforms, sensor networks, body area networks, and critical infrastructure networks. He served as a distinguished lecturer for IEEE COMSOC during the 2023/24 term. Additionally, he holds senior membership in both the IEEE and the National Academy of Inventors in the United States. He received several recognitions and awards, including the US National Science Foundation CAREER award, the 2021 "Innovator of the Year" award by the Henry Samueli School of Engineering at the University of California, Irvine, and two United States Congress certificates of merit, among other recognitions. He has served in numerous editorial roles over the years, as well as an expert reviewer for national and international funding agencies and review boards.

Hüseyin Arslan (Fellow, IEEE) received the B.S. degree from the Middle East Technical University, Ankara, Türkiye, in 1992, and the M.S. and Ph.D. degrees from Southern Methodist University, Dallas, TX, USA, in 1994 and 1998, respectively. From 1998 to 2002, he was with the Research Group, Ericsson Inc., Charlotte, NC, USA, where he was involved with several projects related to 2G and 3G wireless communication systems. Since 2002, he has been with the Electrical Engineering Department, University of South Florida, Tampa, FL, USA, where he is a Professor. In 2013, he joined Istanbul Medipol University, Istanbul, Türkiye, where he is the Dean of the School of Engineering and Natural Sciences. He was a part-time Consultant for various companies and institutions, including Anritsu Company, and the Scientific and Technological Research Council of Turkey (TÜBITAK). He conducts research in wireless systems, with emphasis on the physical and medium access layers of communications. His current research interests are on 5G and beyond radio access technologies, physical layer security, interference management, cognitive radio, multicarrier wireless technologies, dynamic spectrum access, non-terrestrial communications (high altitude platforms), and joint radar (sensing) and communication designs. He was a member of numerous editorial boards and technical committees and held several leadership roles within IEEE and related organizations. He served as an editor for multiple international journals, guest editor for several special issues, and reviewer for many high-impact publications.